

# Statistical analysis of Al III and C III] emission lines as virial black hole mass estimators in quasars

T. M. Buendia-Rios<sup>1</sup>, C. A. Negrete<sup>2</sup>, P. Marziani<sup>3</sup>, and D. Dultzin<sup>1</sup>

<sup>1</sup> Instituto de Astronomía, UNAM, México DF. 04510, Mexico

<sup>2</sup> CONACyT Research Fellow - Instituto de Astronomía, UNAM

<sup>3</sup> INAF, Osservatorio astronomico di Padova, 35122, Padova, Italy  
e-mail: tbuendia@astro.unam.mx

Received ...; accepted ...

## ABSTRACT

**Aims.** We test the usefulness of the intermediate ionisation lines Al III  $\lambda$ 1860 and C III]  $\lambda$ 1909 as reliable virial mass estimators for quasars.

**Methods.** We identify a sample of 309 quasars from the SDSS DR16 in the redshift range  $1.2 \leq z \leq 1.4$  to have [O III]  $\lambda$ 3728 recorded on the same spectrum of Al III  $\lambda$ 1860, Si III]  $\lambda$ 1892, and C III]  $\lambda$ 1909. We set the systemic quasar redshift using careful measurements of [O III]  $\lambda$ 3728. We then classified the sources as Population A, extreme Population A (xA) and Population B, and analysed the 1900 Å blend using multi-component models to look for systematic line shifts of the Al III  $\lambda$ 1860 and C III]  $\lambda$ 1909 along the quasar main sequence.

**Results.** We do not find significant shifts of the Al III  $\lambda$ 1860 line peak in Pop. B and the wide majority of Pop. A. For Pop. xA, a small median blueshift of  $-250 \text{ km s}^{-1}$  was observed, motivating a decomposition of the Al III line profile into a virialized component centred at rest-frame and a blueshifted component for an outflow emission. For Pop. B objects, we proved the empirical necessity to fit a redshifted very broad component (VBC), clearly seen in C III], and analysed the physical implications on a Pop. B composite spectrum using CLOUDY simulations. We find consistent black hole mass estimations using Al III and C III] as virial estimators for the bulk of Population A.

**Conclusions.** Al III (and even C III]) is a reliable virial black hole mass estimator for Pop. A and B objects. xA sources deserve special attention due to the significant blueshifted excess observed in the line profile of Al III, although not as large as those observed in C IV  $\lambda$ 1549.

**Key words.** quasar main sequence – line profiles – emission lines – supermassive black holes –

## 1. Introduction

In 1992, Boroson & Green carried out a principal component analysis (PCA) on a sample of  $\sim 80$  Palomar-Green quasars. Their analysis identified a first eigenvector dominated by an anticorrelation between the [O III]  $\lambda$ 5007 peak intensity and the strength of optical Fe II emission. In this first eigenvector (from now on "Eigenvector 1"; E1), two dimensions, (1) the full width at half maximum of H $\beta$  (FWHM(H $\beta$ )) and (2) the Fe II emission parameterised by the ratio of the equivalent widths of the Fe II emission at 4750 Å and H $\beta$ ,  $R_{\text{FeII}} = \text{EW}(\text{FeII}\lambda 4750)/\text{EW}(\text{H}\beta)$  define what is known as the optical plane of the main sequence of quasars (MS, Marziani et al. 2018). In this way the MS is an empirical sequence based on optical parameters, easy to measure in single-epoch spectra. The spectroscopic trends led Sulentic et al. (2000a) to distinguish two populations: quasars with  $\text{FWHM}(\text{H}\beta) < 4000 \text{ km s}^{-1}$  belongs to Population A (Pop. A), while objects with  $\text{FWHM}(\text{H}\beta) > 4000 \text{ km s}^{-1}$  are Population B (Pop. B).

The E1 gained two more dimensions over the years, becoming the 4DE1 (Sulentic et al. 2000a,c, 2007). The 4DE1 involves optical, UV and X-ray data, and its additional dimensions are (3) the photon index in the soft X-rays domain (below 2 keV),  $\Gamma_{\text{soft}}$  (Wang et al. 1996), and (4) the systematic blueshift of the high-ionisation line C IV  $\lambda$ 1549 (Sulentic et al. 2000d, 2007), spe-

cially prominent among Pop. A objects. The soft X-ray excess (Singh et al. 1985) is a dominant component of the X-ray spectra of many AGN. It was adopted as a critical parameter of the 4DE1 that correlates opposite extremes of populations A and B (Bensch et al. 2015). Sources with higher values of soft X-ray excess (corresponding to a value of the soft-X photon index  $\Gamma_{\text{soft}} \approx 3 - 4$ ) concentrate among the highly accreting Pop. A quasars (Grupe et al. 2004; Sulentic et al. 2007), while Pop. B quasars typically have  $\Gamma_{\text{soft}} \approx 2$ . The most widely-accepted interpretation of the excess detected in soft X-rays is a measure of comptonized emission in a corona connected with the innermost accretion disk (Walter & Fink 1993; Petrucci et al. 2020 and references therein). The systematic high amplitude of the C IV  $\lambda$ 1549 blueshift of quasars with high Eddington ratio may indicate the presence of strong outflows most likely originating in a disc wind (Netzer 2015; Coatman et al. 2016, 2017). Sulentic et al. (2007) introduced the line centroid velocity shift at half-maximum (see Zamfir et al. 2010, for a more detailed description) of C IV as the UV E1 measurement in the 4DE1 parameter space. The observational definition of the accretion and outflow processes is the motivation behind the two additional dimensions. In the following, we shall consider the C IV only, as it is available for most quasars at  $z \gtrsim 1.4$  surveyed by the Sloan Digital Sky Survey (SDSS). The division between the two populations is not enough to reflect the spectral diversity (e.g. Marziani et al. 2010). Sulentic

et al. (2002) made sub-divisions of  $\Delta\text{FWHM}(\text{H}\beta)=4000 \text{ km s}^{-1}$  and  $\Delta R_{\text{FeII}}=0.5$  to emphasise the trends in spectral properties especially seen in Pop. A sources as a function of  $R_{\text{FeII}}$  (Du et al. 2016; Shen & Ho 2014; Sun & Shen 2015, e.g.). This division defines the A1, A2, A3 and A4 bins as  $R_{\text{FeII}}$  increases, and B1, B1+, B1++ (as well as B2, B2+ in the range of  $R_{\text{FeII}}$  0.5-1) as  $\text{FWHM}(\text{H}\beta)$  increases. Spectra belonging to the same bin should have similar characteristics concerning the line profiles and optical and UV line ratios (Sulentic et al. 2007; Zamfir et al. 2010).

A quasar spectrum can be characterised using two physical parameters: the Eddington ratio (defined as the ratio of the bolometric and Eddington luminosities,  $R_{\text{Edd}} = L_{\text{bol}}/L_{\text{Edd}}$ ) and the black hole mass ( $M_{\text{BH}}$ ) which can be only coarsely estimated employing the MS of quasars (Panda et al. 2019b). This is why it is necessary to accurately obtain  $M_{\text{BH}}$  either with the reverberation mapping technique (Netzer & Peterson 1997; Panda et al. 2019a; Dalla Bontà et al. 2020) or with methods based on single-epoch spectra (Shen 2013). The  $M_{\text{BH}}$  relates the evolutionary stage of the quasar with the accretion process (Small & Blandford 1992; Di Matteo et al. 2003; Fraix-Burnet et al. 2017). The knowledge of the  $M_{\text{BH}}$  allows us to assess the strength of the gravitational forces and gain inferences on the dynamics of the region surrounding the black hole (e.g., Ferland et al. 2009; Marconi et al. 2009; Netzer & Marziani 2010). The definition of the virial mass as used in this paper is:

$$M_{\text{BH}} = f \frac{r \delta v_r^2}{G} \quad (1)$$

where  $r$  is the distance of the line emitting gas from the central black hole,  $\delta v_r$  is the line broadening due to virial motions, and  $G$  is the gravitational constant.  $f$  is the virial factor dependent on the geometry, orientation and kinematics of the emitting region (e.g., Peterson et al. 1993; Liu et al. 2017; Mejía-Restrepo et al. 2018). The parameter  $f$  is intended to take into account phenomena that affects the measure of the line broadening (usually FWHM or velocity dispersion) and that may include radiation-pressure effects (Netzer & Marziani 2010; Liu et al. 2017), as well non-virial kinematical components due to outflow or inflow. All methods using optical and UV broad lines are based on estimating the distance of the broad line region (BLR) from the central continuum source,  $r_{\text{BLR}}$ . At low redshift ( $z \leq 0.8$ ), one can estimate  $M_{\text{BH}}$  using  $\text{FWHM}(\text{H}\beta)$  as the  $\delta v_r$ , but as further in redshift we go, the less practical this measure becomes. So few options are left: (1) following the  $\text{H}\beta$  line into the infrared, a feat requiring large telescopes and IR spectrometers or (2) adopting other broad lines (e.g.  $\text{MgII}\lambda 2800$ ,  $\text{AlIII}\lambda 1860$  or  $\text{CIV}\lambda 1549$ ) as surrogate virial estimators if  $z > 1$ .

The use of  $\text{CIV}\lambda 1549$  emission line in the UV as a virial mass estimator is problematic due to the strong blueshift with respect to the rest frame frequently observed (Richards et al. 2011, and references therein), associating the high ionisation line (HIL  $\geq 40 \text{ eV}$ ) to outflowing winds (Gaskell 1982; Marziani et al. 1996). This outflow indicates that the emitting gas is not in virial equilibrium and therefore is not a reliable mass indicator due to the systematic biases. Other HILs such as  $[\text{OIII}]\lambda\lambda 4959, 5007$  could also present blueshifts arising from an outflowing gas (Zamanov et al. 2002), possibly associated with a disc wind. Hence, the narrow-line region (NLR) in sources showing spectroscopic blue shifts is not likely to be dynamically related to the gravitational potential of the host galaxy. To avoid systematic shifts in the velocity dispersion estimates (as well as in the proper rest frame), the width of  $[\text{SiII}]\lambda\lambda 6716, 6731$  or the doublet  $[\text{OII}]\lambda\lambda 3727, 3729$  (hereafter  $[\text{OII}]\lambda 3728$ ) has been proposed as

an alternative to  $[\text{OIII}]\lambda\lambda 4959, 5007$  (Komossa & Xu 2007; Salvander et al. 2007). Narrow low ionisation lines (LILs) serve as better rest frame references, as they provide a value closest to the one of the host galaxy (Marziani & Sulentic 2012; Bon et al. 2020).

To avoid the HILs in the UV spectral range we propose to work with the LILs or the intermediate ionisation lines (IILs  $\sim 20\text{-}40 \text{ eV}$ ). A possible strategy is to use high signal-to-noise ratio (S/N) of  $\text{H}\beta$  as a template to model the IILs  $\text{AlIII}\lambda 1860$  and  $[\text{SiIII}]\lambda 1892$  (among others). Velocity-resolved reverberation mapping (Bentz et al. 2009; Denney et al. 2010; Feng et al. 2021) detect inflow and outflow motions, although the effects seem to be relatively minor as far as the width of the LILs is concerned. We emphasise the importance of finding a reliable virial mass estimator in the UV range that is paired to LIL  $\text{H}\beta$  and we propose the surrogate lines  $\text{AlIII}$  and  $[\text{CIII}]$  present in the 1900Å blend. The blend includes the IILs:  $\text{AlIII}\lambda 1860$ ,  $[\text{SiIII}]\lambda 1892$  and  $[\text{CIII}]\lambda 1909$ .  $\text{AlIII}\lambda 1860$  is a resonant doublet ( ${}^2P_{3/2,1/2}^o \rightarrow {}^2S_{1/2}$ ) in the sodium isoelectronic configuration, while  $[\text{SiIII}]\lambda 1892$  and  $[\text{CIII}]\lambda 1909$  are due to the inter-combination transitions ( ${}^2P_1^o \rightarrow {}^1S_0$ ) with widely different critical densities ( $\approx 2 \times 10^{12} \text{ cm}^{-3}$  and  $3.2 \times 10^9 \text{ cm}^{-3}$ , respectively; Negrete et al. 2012; Marziani et al. 2020). The parent ionic species imply ionisation potentials intermediate between LILs and HILs.

The usefulness of  $[\text{SiIII}]$  and  $\text{AlIII}$  as virial estimators is suggested by their profiles showing consistent width and shape with the one of  $\text{H}\beta_{\text{BC}}$  (Marziani et al. 2010, 2022). They are symmetric and are usually not affected by strong outflows often observed in the  $\text{CIV}\lambda 1549$  profile (Marziani et al. 2017; Martínez-Aldama et al. 2018). The rest-frame of the 1900Å blend based on the quasar redshift derived from the  $[\text{OII}]\lambda 3728$  line (Bon et al. 2020) would prove the effectiveness of  $\text{AlIII}$  and  $[\text{CIII}]$  as virial broadening estimators in the absence of systematic blueshifts.

The main objective of the present work is (1) to test the consistency of the  $\text{AlIII}$  and  $[\text{CIII}]$  emission lines with the systemic redshift derived from the  $[\text{OII}]$  line and in the case of a systematic shift is found, to propose a correction; and (2) to probe the usefulness of the IILs  $\text{AlIII}$  and  $[\text{CIII}]$  as reliable virial mass estimators. The outline of the paper is as follows. Section 2 is a description of the sample and employed selection criteria. Section 3 describes the analysis of the redshift estimation as well as the multi-component fitting of the 1900Å blend and  $[\text{OII}]\lambda 3728$  region. In Section 4 we present our results for the entire sample and by populations, analysing the trends and correlations obtained along with the physical parameters. Section 5 discusses the virial  $M_{\text{BH}}$  obtained from  $\text{AlIII}$  and  $[\text{CIII}]$ , virial luminosity estimates for the extreme Population A sub-sample, and the inter-comparison between  $\text{CIV}$  and  $\text{AlIII}$ , along with a schematic interpretation of the  $\lambda 1900$  blend in Population B. Section 6 provides the summary and conclusions.

## 2. Sample description

The spectroscopic quasar sample used in this work was selected from the SDSS data release 16 (DR16, Lyke et al. 2020), limited with the following filters: (1)  $1.2 < z < 1.4$  to cover the 1900Å blend and the  $[\text{OII}]\lambda 3728$  doublet line simultaneously; and (2) high  $\text{S/N} > 20$  (measured in the continuum range around 1700Å) to be able to decompose the blend at 1900Å. These criteria give us a sample of 1379 objects.

Not all spectra have a visible  $[\text{OII}]$  emission. To determine the visibility of  $[\text{OII}]$  in the selected objects, we use a third criterion applied to all spectra normalised by a continuum region

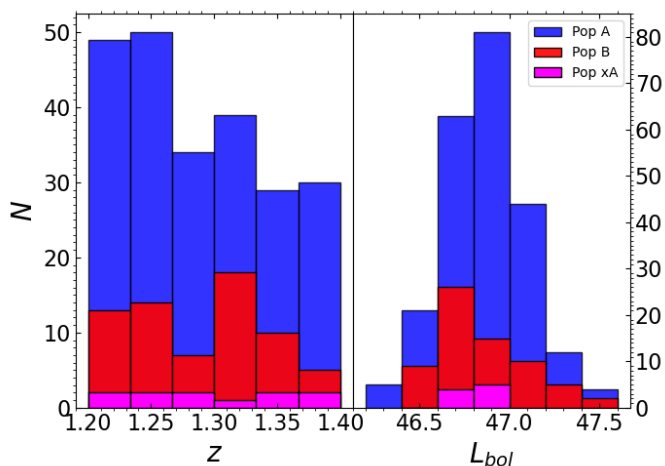


Fig. 1: Distribution of redshift (left) and of bolometric luminosity (right) for the total sample (309 objects). Colour code: Pops. A, xA and B in blue, magenta and red, respectively.

around the line: (3) the ratio  $f_{[\text{OII}]}$  defined as the intensity ratio of  $[\text{OII}]$  in the range 3722–3734Å ( $F([\text{OII}]$ ), and the observed continuum over the range 3670–3700Å ( $F(\text{cont})$ , composed of the AGN continuum and strong FeII emission contaminating the region),  $f_{[\text{OII}]} = [F([\text{OII}]) + F(\text{cont})]/F(\text{cont})$ , with the constriction of  $f_{[\text{OII}]} > 1.3$ . Only 309 spectra satisfied this last condition.

$[\text{OII}]\lambda 3728$  is a relatively weak line that is also affected by the emission of the FeII multiplet (e.g. Vanden Berk et al. 2001). The fact that  $[\text{OII}]\lambda 3728$  was detected in only 22% of the objects in the initial sample (with S/N > 20) may be due to two reasons. The first one is that it may be severely contaminated by sky subtraction residuals, whose emission is strong at the red end of the spectra. The second reason is attributed to the intrinsic  $[\text{OII}]\lambda 3728$  emission. We already know the trends of the MS in regards to oxygen, in Sulentic et al. (2000a, right panel of their Figure 2) it is very clear that for Pop. A quasars the oxygen is fainter than in Pop. B, and decreasing along the sequence, indicating that the higher the accretion (bins A3–A4), the less prominent oxygen lines we are observing (Sulentic et al. 2000a; Shen & Ho 2014). So, discarding spectra with no detectable  $[\text{OII}]\lambda 3728$ , creates a bias against highly accreting sources.

The next step was to separate Pops. A and B (Sec. 3.3). For this purpose, it was necessary to apply the luminosity dependent criterion of Sulentic et al. (2017) which brings the limit at  $\text{FWHM} \approx 4000 \text{ km s}^{-1}$  to significantly higher values for sources of bolometric luminosity  $\log L_{\text{bol}} \geq 46 \text{ ergs s}^{-1}$ :  $\text{FWHM}_{\text{AB}} \approx 3500 + 500(L_{\text{bol}}/3.69 \times 10^{44})^{0.15} \text{ km s}^{-1}$  (applied to the CIII] line) to separate Pop. A and B. In our sample, Pop. A  $\text{FWHM}(\text{AlIII}\lambda 1860)$  goes from  $\sim 2500 \text{ km s}^{-1}$  to almost  $4500 \text{ km s}^{-1}$ , and only one source had a value less than  $2000 \text{ km s}^{-1}$  (Sec. 4.2).

Afterwards, we looked for extreme Pop. A sources (xA or highly accreting quasars) using the UV line ratios from Marziani & Sulentic (2014, hereafter MS14):  $\text{AlIII}\lambda 1860/\text{SiIII}\lambda 1892 \geq 0.5$  and  $\text{CIII}\lambda 1909/\text{SiIII}\lambda 1892 \leq 1$  (see Section 3.3 for a more detailed description), finding 11 xA quasar candidates.

The median value of the S/N distribution of our final sample is  $\approx 31$ . The redshift distribution is reported in Figure 1 (left). The  $z$ -range is small, due to the values of the line wavelength range needed to have both AlIII and  $[\text{OII}]$  recorded on the same spectrum: AlIII is at the blue edge and  $[\text{OII}]$  at the red edge of

each spectrum (see Figure 2, upper panel, for an example). This  $z$  range is the most relevant condition to ensure that the systemic redshift of the quasar is measured precisely (see also Section 3.1). In Figure 1 (right), the  $L_{\text{bol}}$  distribution of our sample shows that our sample is made of luminous AGN. The luminosity median values are  $\log L_{\text{bol}} = 46.8 \text{ ergs s}^{-1}$  for Pop. A objects (including xA quasars), and  $\log L_{\text{bol}} = 46.6 \text{ ergs s}^{-1}$  for Pop. B. Previous works usually found 50% Pop. A and 50% Pop. B in flux-limited samples (Zamfir et al. 2010; Marziani et al. 2013). The larger sample size of Pop. A might be due to the flux limit of the Sloan survey along with the relatively high redshift  $z \sim 1$  (Sulentic et al. 2014) that might have caused a Malmquist-type bias yielding an excess of Pop. A sources (i.e., radiating at relatively high Eddington ratio) with respect to Population B (radiating at lower Eddington ratio).

### 3. Data analysis

Optical spectral data used in this work were wavelength- and flux-calibrated by the SDSS DR16 pipeline. For the Galactic dust extinction, we use the reddening estimates from Schlafly & Finkbeiner (2011) assuming the value of the  $R_V$  coefficient as 3.1. The Galactic absorption median value was  $\mu_{\frac{1}{2}}(A_B) \approx 0.14$ , ranging from 0.03 up to  $\sim 0.6$ . We choose to apply this correction only in correspondence of the redshifted 1900Å blend, where the median  $A_B$  implies a flux increase of 14%. The chosen value only affected the luminosity computation, not the spectral slope between the blue and red edge of the 1900Å blend. Redshift and flux corrections of the spectra were first done using the  $z$  values provided by the SDSS DR16. An additional  $z$  correction was applied using the rest-frame estimated with the  $[\text{OII}]\lambda 3728$  line, as described below.

#### 3.1. $[\text{OII}]\lambda 3728$ redshift estimation

The SDSS redshift estimates can be biased (Hewett & Wild 2010). We observed discrepancies between the peak and rest-frame wavelength of  $[\text{OII}]$  (as seen in Figure 2) after the SDSS-based  $z$  correction. We applied an additional redshift correction using the peak intensity wavelength of  $[\text{OII}]\lambda 3728$  as described in Section 3.2.2 with a more carefully fitting using the `specfit` task (Kriss 1994) from Image Reduction and Analysis Facility (IRAF, Tody 1986).

We compare the differences between the SDSS DR16 redshift and the  $z$  values obtained from the narrow line  $[\text{OII}]$  in Figure 2. The median value of  $\Delta z = z_{[\text{OII}]} - z_{\text{SDSS}} = 4.918 \times 10^{-4}$  (roughly  $\sim 70 \text{ km s}^{-1}$  in the rest frame, green dotted line of the Figure 2) indicates that the SDSS- $z$  values were underestimated. A fraction of the objects,  $\sim 25\%$  of the sample, showed a difference in the rest-frame  $z$  higher than  $150 \text{ km s}^{-1}$  (up to  $\sim 450 \text{ km s}^{-1}$ ). The distribution is not symmetric around the median value. The main reason of these systematic differences is probably a bias of the SDSS due to the usage of HILs.

#### 3.2. Multicomponent fitting

The UV range covered in the sample is populated by blended, intermediate ionisation lines. To analyse the emission lines of the spectra, multi-component fits were done using the task `specfit`. This routine allows us to simultaneously fit all components present in the spectrum: continuum, FeII features, and emission lines, computing the  $\chi^2$  parameter that measures the difference between the original spectra and the fitted one. The task

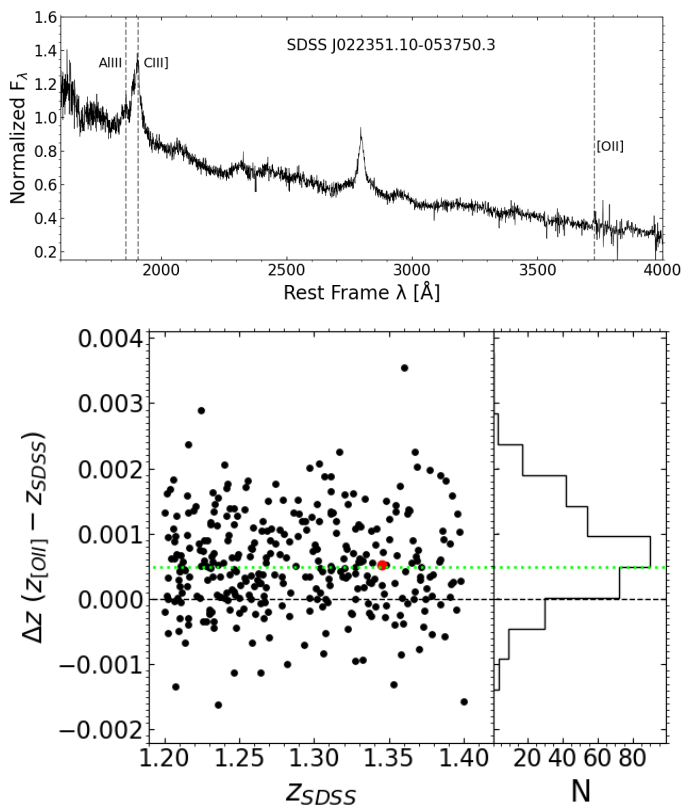


Fig. 2: *Upper panel*: Example of a spectrum from our sample. Vertical lines are the prominent emission lines of our work: AlIII $\lambda$ 1860, CIII $\lambda$ 1909 and [OII] $\lambda$ 3728. Abscissa scale is rest-frame wavelength in  $\text{\AA}$ . Ordinate scale is the normalised flux at 1700  $\text{\AA}$ . *Lower left panel*:  $z_{\text{SDSS}}$  vs.  $\Delta z$  for the sample. The red point corresponds to the values of  $\Delta z$  and  $z$  of the upper panel spectrum. *Lower right panel*: Distribution of  $\Delta z$ . The lime line shows the shift  $\Delta z$  median value:  $4.918 \times 10^{-4}$  equivalent to  $\sim 65 \text{ km s}^{-1}$ .

`specfit` minimises the  $\chi^2$  to find the best fit. Intensity measures of [OII] $\lambda$ 3728 were carried out with the `splot` task within IRAF.

The primary continuum source in the UV region is well known to be originated from the accretion disk (e.g., Malkan & Sargent 1982; Wandel & Petrosian 1988; Capellupo et al. 2016). In the absence of extinction, the most widely-used model for the continuum is a single power-law over a limited spectral range (see e.g., Śniegowska et al. 2020). We fitted a local continuum for two spectral ranges centred on the 1900  $\text{\AA}$  blend and [OII] $\lambda$ 3728, the most important emission lines relevant to this work (see Figure 3).

Along the E1 main sequence, it is possible to model the H $\beta$  line profile with three components with blueshifted, unshifted and redshifted centroids (blue [BLUE], broad [BC] and very broad components [VBC], respectively; Marziani et al. 2010). Then, we can use this model for all strong broad lines by varying the relative intensity of the components. The model considering the BC and VBC separation applies to Pop. B sources and is consistent with stratification of the BLR (Sulentic et al. 2000b; Snedden & Gaskell 2007; Wolf et al. 2020). The BC (hydrogen density  $n_{\text{H}} \sim 10^{12} \text{ cm}^{-3}$ , ionisation parameter  $\log U \sim -2$  and column density  $N_{\text{c}} \gtrsim 10^{23} \text{ cm}^{-2}$ ) is present in almost all type-1 quasars and corresponds most likely to the virialized part of the BLR, while the VBC can be interpreted as the emitted gas in

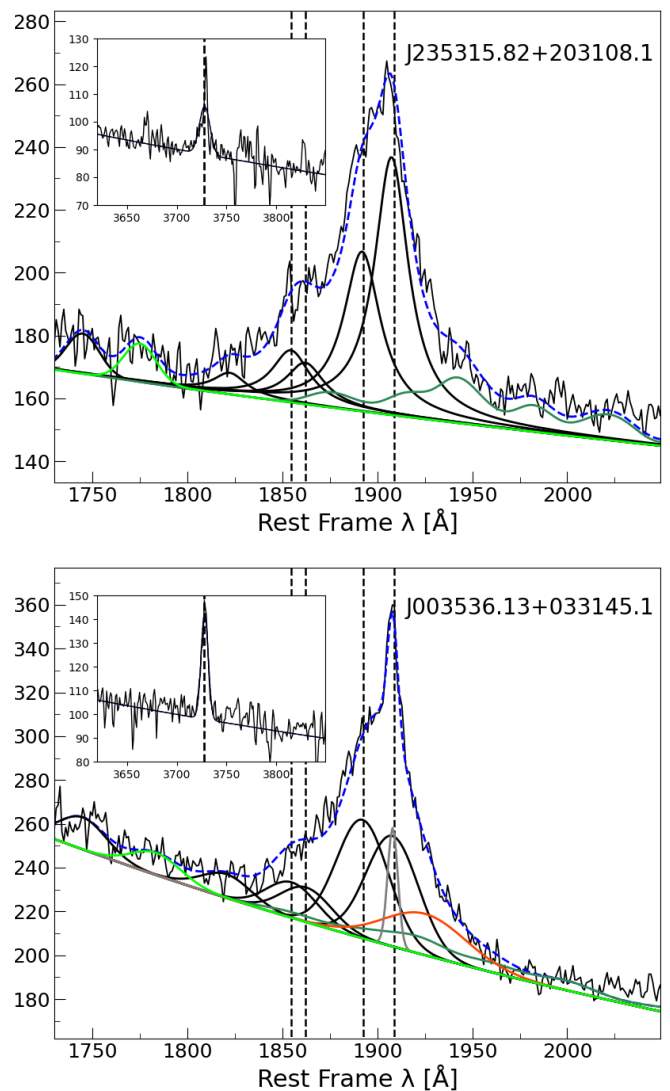


Fig. 3: Analysis of the 1900 $\text{\AA}$  blend and the [OII] $\lambda$ 3728 region (small box within the Figure) as described in section 3.2. Abscissa scale is rest-frame wavelength in  $\text{\AA}$ . Ordinate scale is the specific flux in units of  $10^{-17} \text{ ergs s}^{-1} \text{ cm}^{-2} \text{ \AA}^{-1}$ . *Top*: Example of a Pop. A source fitted with a Lorentzian profile. *Bottom*: Example of a Pop. B source fitted with a Gaussian profile. The black lines identify the BC of AlIII $\lambda$ 1860, SiIII $\lambda$ 1892 and CIII $\lambda$ 1909 (red and grey are the VBC and NC of CIII $\lambda$ 1909 respectively if present). The dashed blue line is the multi-component model obtained by `specfit`. Green lines trace the adopted FeII (pale) and FeII template (dark).

the innermost BLR (e.g., Sulentic et al. 2000b; Marziani et al. 2003a, 2010; Wang & Li 2011; Wolf et al. 2020). The BLUE component is apparent as a blueshifted excess superimposed to the blue wing of the BC (Leighly & Moore 2004).

The 1900 $\text{\AA}$  blend contains the same emission lines for both Pop. A and B: AlIII, SiIII, and CIII $\lambda$ 1909 which are the strongest features (see also Table 1 from Negrete et al. 2012). Figure 3 shows example fits of a Pop. A and B sources, where we used a Lorentzian function for Pop. A and a Gaussian function for Pop. B. For Pop. B spectra, we included an additional Gaussian component for the VBC. A detailed description of the phenomenology of the line profiles can be found in Sulentic et al. (2000a,

2002); Marziani et al. (2022) and references therein. More in detail, we consider the following components described in Sections 3.2.1 and 3.2.2 for a complete model of each spectrum

### 3.2.1. Region 1: 1750-2050Å.

1. *Continuum*: We adopt a single power-law to fit the region 1700-2050Å, using a continuum window at 1700 Å as seen in Francis et al. (1991).
2. *FeII and FeI*: Emission of the FeII multiplets can be strong in the vicinity of CIII]λ1909, as seen in the average quasar spectrum from Vanden Berk et al. (2001). They appear to be strong when AlIII is also strong (Hartig & Baldwin 1986). Strong FeII and AlIII emission further strengthen the conclusion that the BLR densities, at least in Pop. A sources are very high (on the basis of photoionisation models,  $\sim 10^{11} - 10^{12} \text{ cm}^{-3}$ , Korista et al. 1997a; Kuraszewicz et al. 2000). We adopted for the FeII template model the one obtained by Vestergaard & Wilkes (2001). The specfit task scaled and broadened the template to reproduce the observed emission (Boroson & Green 1992). In most cases, we fitted the multiplet FeII UV191 (seen in the blue-ward of the 1900Å blend, Moore 1945) as an isolated Gaussian in the rest-frame. We adopted a Gaussian profile because the feature is a blend of several individual FeII lines belonging to the same multiplet. If the FeII multiplet is prominent, an extra component is added: FeIIλ1914 to fit an excess seen near the red wing of CIII]λ1909 associated with unresolved FeII template emission in Pop. A quasars (Negrete et al. 2012). This FeIIλ1914 emission is a single line, so we fitted it using a Lorentzian profile to be consistent with the profile of the BCs. The spectrum of I Zw 1 shows this effect: both CIII] and FeIIλ1914 are needed to account for the double-peaked feature at 1910Å that is too broad to be explained by a single line (Negrete et al. 2012, 2013). This criterion rests on the assumption that FeIIλ1914 and the FeII UV multiplet #191 are enhanced by Lyα fluorescence (Sigut & Pradhan 1998; Johansson et al. 2000).
3. *CIII]λ1909*: Strengths and FWHM were left free to vary in the specfit model with one restriction:  $\text{FWHM}(\text{CIII]}\lambda 1909) \leq \text{FWHM}(\text{AlIII}\lambda 1860)$  or  $\text{FWHM}(\text{SiIII}\lambda 1892)$  to avoid a divergence of the  $\text{FWHM}(\text{CIII]}\lambda 1909)$  due to the FeII emission on the red side of the blend. In the case where the model does not successfully follow this condition, the FWHM of both lines were forced to be the same to avoid a larger  $\text{FWHM}(\text{CIII]})$ . We also added a narrow component (NC) if needed with a fixed upper limit of  $\text{FWHM} \sim 1000 \text{ km s}^{-1}$  at the rest-frame wavelength as an initial condition. The distribution of the peak emission around 1909 Å shows a fraction of quasars with a shorter wavelength than the one expected for the laboratory wavelength of CIII]λ1909 (Figure 4). This phenomenon could be due to two main reasons. First, we are looking at the prohibited line [CIII]λ1906 (dotted line, Figure 4) also observed in the NLR. Second, a blueshifted emission of CIII] NC due to an outflow in the NLR. For Pop. B objects we included a redshifted VBC whose strengths and FWHM were left free to vary with a FWHM lower limit  $\approx 7000 \text{ km s}^{-1}$ . In Figure 5 we illustrate the necessity of using an additional component in the CIII] profile. Looking at the residuals and the  $\chi^2$  values, the best fit (according to the F distribution for the ratio of the  $\chi^2$ , Bevington & Robinson 2003) is the one with the VBC as seen for

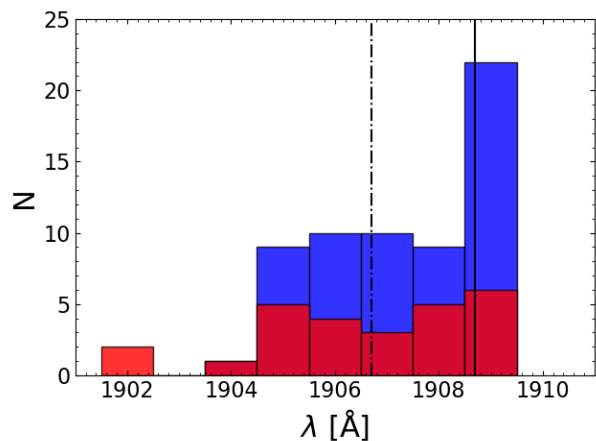


Fig. 4: Distribution of the peak blend wavelength around 1909Å, for Pop. A (blue) and Pop. B (red). The vertical lines identify the rest-frame wavelength of [CIII]λ1906 (dotted) and CIII]λ1909 (filled).

the SDSS spectrum J012726.39+154153.8 with a  $\chi^2_{\text{VBC}} \approx 0.1676$  in contrast to  $\chi^2 \approx 0.4451$  obtained without VBC, respectively (see section 5.4 for its interpretation).

4. *SiIII]λ1892*: Strengths and shifts were free to vary, with one restriction:  $\text{FWHM}(\text{SiIII]}\lambda 1892) \geq \text{FWHM}(\text{CIII]}\lambda 1909)$ . We had some difficulties due to the nature of the blend itself. The line tended to be blueshifted in order to “fill” its blue side, and therefore, AlIII1860 also presented a blueshift as seen in Martínez-Aldama et al. (2018). In the cases where the shift was completely unreal under a visual inspection, we fixed the central wavelength of SiIII] to the rest-frame.
5. *AlIII1860*: The doublet was resolved and the blue component shifts, FWHM, and intensity were allowed to vary, with the red one tied to the blue by identical FWHM and fixed wavelength ratio. The ratio between the intensity of the red and blue component of the doublet was kept fixed 0.8 (Laor et al. 1997). Rarely, a different ratio up to 0.98 was assumed according to be observed doublet profile. However doublet total strengths and shifts were left free to vary. Regarding CIII]λ1909, the condition  $\text{FWHM}(\text{AlIII}\lambda 1860) \geq \text{FWHM}(\text{CIII]}\lambda 1909)$  was imposed. The  $\text{FWHM}(\text{CIII]})$  limit comes from the low value of the CIII]λ1909 critical density. On the converse the AlIII line, emitted via a permitted transition, has no well-defined critical density (Baldwin et al. 1995; Korista et al. 1997a).
6. *Other lines*: Two lines not as prominent as those described above in points 3-5 were detected in the blue side of the 1900Å blend: NIII]λ1750 and SiIIλ1816. We assumed them to be at the rest-frame as an initial condition, although their shifts, strength and FWHM were left free to vary.

### 3.2.2. Region 2: 3550-3950Å.

The [OII]λ3728 doublet emission line is one of the main emission features of this spectral range. Hence, the components are the same for all spectra:

1. *Continuum*: A strong pseudo-continuum associated with FeII emission is expected to be present in the spectral range around [OII]λ3728 between 3500 Å and 3850 Å (Vanden Berk et al. 2001). However, the limited range 3700-3770 Å

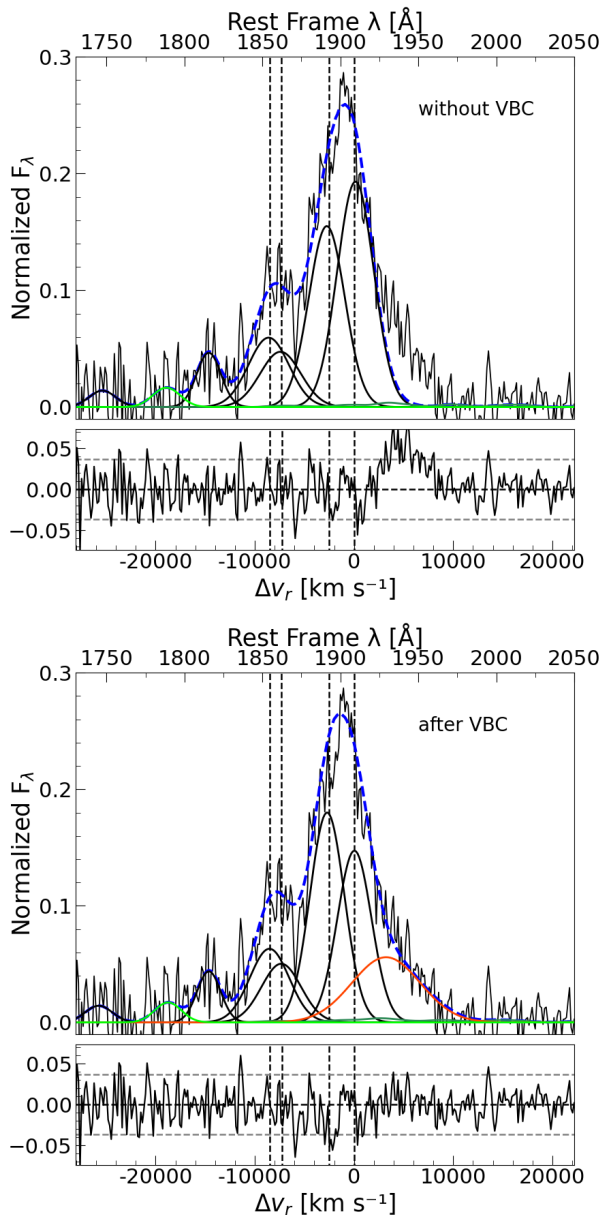


Fig. 5: Analysis of the 1900Å blend (continuum extracted for simplicity in both spectra) of SDSS J012726.39+154153.8 as described for Figure 3. C $\text{III}$ ] profile fitted with only a BC and BC+VBC, top and bottom, respectively. Abscissa is rest-frame wavelength in Å. Ordinate is the normalised specific flux obtained from *specfit*.

is smooth enough to permit the use of a power-law to model the sum of the AGN continuum and the FeII emission.

2. [O $\text{II}$ ] $\lambda$ 3728: Our spectra have unresolved or almost unresolved [O $\text{II}$ ] $\lambda$ 3727,3729 lines because the spectral resolution at the observed wavelength around 8200 Å is  $\lambda/\delta\lambda \approx 2250$ , so the spectral purity is 3.64 Å, which is larger than the doublet separation. Therefore, we used a single Gaussian fit (Bon et al. 2020).

### 3.3. Spectral types along the E1

In order to classify the objects, we attempted to use as a first approximation the Sulentic et al. (2000c) spectral types. However,

this classification is based on the FWHM H $\beta$  that increases systematically for higher  $L$  objects, and we expect the same effect for the IILs. We identify 242 and 67 Pop. A and B objects, respectively. In a few cases, we had fits with both profiles, almost  $\sim 5\%$  of the sample, but with different FWHM(C $\text{III}$ ]). For these sources, with a value of FWHM near the 4000 km s $^{-1}$  limit, it was necessary to choose the best fit according to the  $\chi^2$  values using the F distribution (Bevington & Robinson 2003). To separate highly accreting candidates of spectral type A3 and A4 (xA) from the A1-A2 sources defined in Sec. 1, we used the UV diagnostics ratios of MS14. Pop. A quasars located at the extreme of the MS, are considered to be sources radiating close to the Eddington if they satisfy the following criterion (e.g., Du et al. 2016):

$$R_{\text{FeII}} = \frac{\text{EW}(\text{FeII}\lambda 4750)}{\text{EW}(\text{H}\beta)} \geq 1.0 \quad (2)$$

An equivalent condition has been proposed at intermediate to high redshift ( $z \gtrsim 1$ ) where the H $\beta$  line is no longer visible in the optical range, using the 1900Å emission line blend of Al $\text{III}$  $\lambda$ 1860, Si $\text{III}$ ] $\lambda$ 1892 and C $\text{III}$ ] $\lambda$ 1909 (MS14). The blend involving these lines constrains the physical conditions in the broad-line emitting gas the same way as extreme optical FeII emission. Measures of high S/N spectra of MS14 yield the selection criterion based on two related ratios:

1. Al $\text{III}$  $\lambda$ 1860/Si $\text{III}$ ] $\lambda$ 1892  $\geq 0.5$  and
2. C $\text{III}$ ] $\lambda$ 1909/Si $\text{III}$ ] $\lambda$ 1892  $\leq 1.0$

The emitting region of the IILs corresponds to the densest emitting region likely associated with the production of LILs like the CaII IR triplet (Matsuoka et al. 2008) and FeII (Baldwin et al. 2004).

We made a bin separation for the bins A1-A2 which we call Pop.  $\tilde{\text{A}}^1$  and the A3-A4 bins will be our Pop. xA candidates. In Figure 6 we show the A1-A2 bins in blue, and in magenta we identify 11 xA quasars.

## 4. Results

Table B.1 of Appendix B lists the results of the line fitting procedures of Sec. 3.2, and the luminosity and  $M_{\text{BH}}$  computations of Section 5. The Table also reports the redshift from the SDSS and our  $z$  estimation using [O $\text{II}$ ], the continuum flux and the normalisation at 1700Å, and the line profile classification (Lorentzian or Gaussian). From the *specfit* analysis we report the intensity, FWHM, shift from the restframe, and EW for each emission line of the 1900Å blend. For the [O $\text{II}$ ] region, we report the intensity and FWHM. The last part of Table B.1 contains the UV diagnostic ratios, black hole mass, Eddington ratio, and virial luminosity (computed only for xA sources, see Sec. 5.2). Table 1 presents a summary of the physical parameter values where we report the median and average values by Population. The reported uncertainties are the semi-interquartile ranges (sIQR) of the parameter distributions. For luminosity estimates we adopted an uncertainty of 10%.

We organise the presentation of our results on line widths and shifts of the 1900Å blend along the MS, separating Pops.  $\tilde{\text{A}}$  (A1-A2), xA and B. The MS is expected to trace changes in the dynamical and physical conditions inside the quasars (Marziani

<sup>1</sup> Note that in previous work Pop. A includes spectral types A1-A2 and A3-A4.

Table 1: Average and median values of the sample physical parameters by population.

	Pop $\tilde{A}$ (231 quasars)		Pop xA (11 quasars)		Pop B (67 quasars)		Notes
	Average	Median	Average	Median	Average	Median	
FWHM(CIII] BC)	3330±280	3370±280	3280±255	3420±260	4490±180	4380±180	<i>a</i>
FWHM(CIII] VBC)	-	-	-	-	8120±410	8120±410	<i>a</i>
FWHM(AlIII)	3560±270	3550±230	3560±230	3530±250	5270±240	5300±250	<i>a</i>
EW (CIII])	-15.43±2.90	-14.77±2.90	-8.33±1.88	-8.94±1.88	-7.18±1.76	-6.97±1.76	<i>b</i>
EW (AlIII)	-3.55±0.94	-3.27±0.94	-7.08±0.79	-7.05±0.79	-5.02±0.97	-4.92±0.97	<i>b</i>
AlIII/SiIII]	0.48±0.11	0.45±0.11	0.63±0.02	0.60±0.02	-	-	<i>c</i>
CIII]/SiIII]	2.17±0.58	1.88±0.58	0.72±0.10	0.75±0.10	0.94±0.22	0.86±0.22	<i>c</i>
CIII](BC+VBC)/SiIII]	-	-	-	-	1.68±0.32	1.53±0.32	<i>d</i>
shift CIII]	50±190	40±190	80±120	50±120	80±90	160±90	<i>a</i>
shift AlIII]	-30±120	10±120	-200±232	-240±230	30±120	10±120	<i>a</i>
log M <sub>BH</sub> (CIII]BC)	8.82±0.14	8.81±0.14	8.79±0.13	8.82±0.13	9.15±0.12	9.13±0.12	<i>e</i>
log M <sub>BH</sub> (AlIII)	8.80±0.10	8.78±0.10	8.79±0.09	8.83±0.09	9.14±0.11	9.12±0.11	<i>e</i>
log L <sub>1909</sub>	47.20	47.19	46.92	46.93	46.84	46.83	<i>f</i>
log L <sub>1860</sub>	46.56	46.56	46.87	46.79	46.73	46.70	<i>f</i>
log L <sub>Bol</sub>	46.87±2.65	46.86±2.65	46.85±1.84	46.87±1.84	46.84±2.59	46.79±2.59	<i>g</i>
R <sub>Edd</sub> (CIII])	0.95±0.20	0.85±0.20	0.98±0.24	0.87±0.24	0.39±0.07	0.39±0.07	<i>h</i>
R <sub>Edd</sub> (AlIII)	0.96±0.19	0.86±0.19	0.91±0.13	0.85±0.13	0.41±0.07	0.39±0.07	<i>h</i>
log L <sub>vir</sub>	-	-	47.09	47.08	-	-	<i>i</i>

**Notes.** <sup>(a)</sup> In units of km s<sup>-1</sup>. <sup>(b)</sup> Rest-frame equivalent widths reported with normalised spectra at 1700Å are in units of Å. <sup>(c)</sup> UV diagnostic ratios from MS14 for Pop. A sources. <sup>(d)</sup> UV diagnostic ratio from MS14 for Pop. B sources. <sup>(e)</sup> Log of M<sub>BH</sub> are computed using the scale relations by M22 in units of M<sub>⊙</sub>. <sup>(f)</sup> Log of Line luminosity in units of ergs s<sup>-1</sup>; uncertainties are the 10% of the value. <sup>(g)</sup> Log of bolometric luminosity in unit of ergs s<sup>-1</sup> computed using the continuum window at 1700Å. <sup>(h)</sup> R<sub>Edd</sub> is the Eddington ratio. <sup>(i)</sup> Log of virial luminosity in units of ergs s<sup>-1</sup>; uncertainties are the 10% of the value.

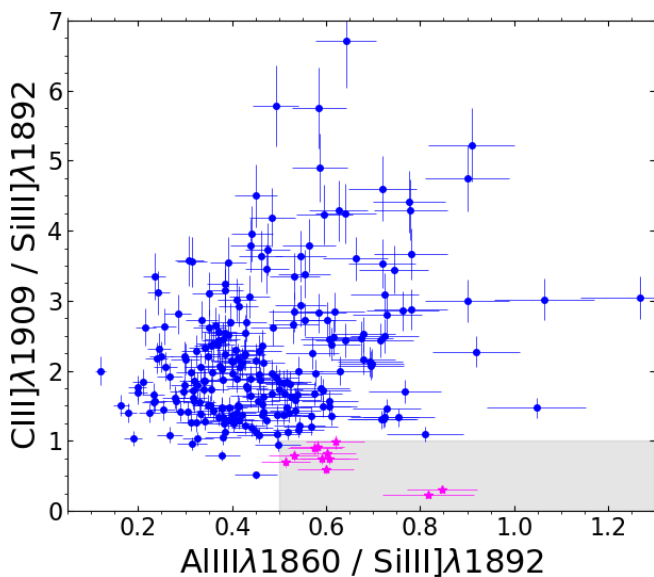


Fig. 6: Distribution of Pop. A sources in the plane defined by the ratios CIII]λ1909/SiIII]λ1892 vs. AlIIIλ1860/SiIII]λ1892. The blue dots are quasars within populations A1-A2 (Pop.  $\tilde{A}$ ) and the xA sources are in magenta located in the lower-right grey area.

et al. 2003a; La Mura et al. 2009; Popović et al. 2019). Line widths (e.g., FWHMs) of LILs and IILs measure the kinematics of the BLR. We assume that Doppler motions in a virialized region produce unshifted and symmetric line broadening. Wavelength shifts of AlIIIλ1860 and CIII]λ1909 were measured

with respect to the [OIII]λ3728 rest frame. They may be due to Doppler effect because of radial gas motions plus obscuration along our line of sight. The differences in line widths observed in the same spectrum might be due to emissions from regions of non-virialized motions (e.g., outflows), as usually seen in Pop. A and also in high luminosity Pop. B objects at high luminosity (Sulentic et al. 2017). Line width differences in type 1 quasars are also associated with the stratification of the emitting region, where broader lines trace the kinematics of the regions closer to the SMBH (e.g., Sulentic et al. 2000b; Peterson & Wandel 2000; Snedden & Gaskell 2007; Wolf et al. 2020; Li et al. 2021). Last, FWHM differences may be due to different orientations of the accretion disk (expected to provide the reference plane of symmetry of the BLR) with respect to our line of sight.

#### 4.1. Systematic shifts

In the virialized region one can expect a modest shift ( $\lesssim |\pm 200|$  km s<sup>-1</sup>) associated with the measurement of the uncertainties. We consider  $\pm 200$  km s<sup>-1</sup> as an uncertainty limit, given the instrumental resolution of the SDSS spectra at their blue side, which is where the 1900Å blend falls in the observed rest frame. Considering our complete sample, the median values of the AlIII and CIII] shifts in the histograms of Figure 7a,c are  $10 \pm 120$  km s<sup>-1</sup> and  $40 \pm 190$  km s<sup>-1</sup>, respectively (see also Table 1). In almost 90% of Pop.  $\tilde{A}$  and B AlIII profiles we find that the shifts are lower than the uncertainty limit. However, Figure 7a shows an asymmetric distribution of AlIIIλ1860 shifts with an extended tail of blueshifts reaching several hundred km s<sup>-1</sup>. Blueshifts larger than 200 km s<sup>-1</sup> imply that we are most likely looking at a mixture of two non-resolved components in the line profiles: a

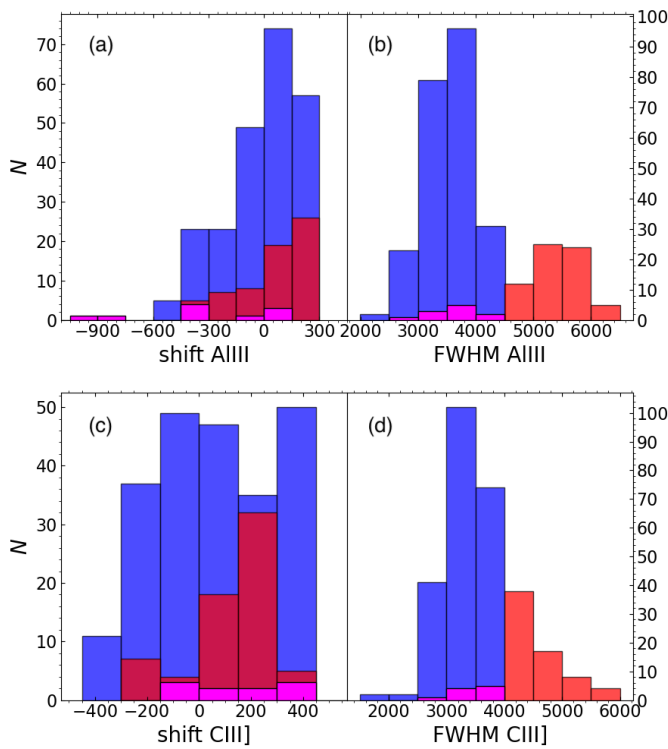


Fig. 7: *Upper*: Distribution of shift with respect to rest-frame and FWHM of  $\text{AlIII}\lambda 1860$ . *Bottom*: same but with  $\text{CIII]}\lambda 1909$ . Shift and FWHM in units of  $\text{km s}^{-1}$ . Colour-code as Figure 1.

virialized plus an outflow component. Even though a blueshifted component in  $\text{AlIII}$  may not be as intense as the blue component of  $\text{CIV}\lambda 1549$  it is essential to be aware of its presence: significant shifts would introduce a bias in the estimation of the rest-frame, as the  $\text{AlIII}$  blue component would broaden and shift the full profile. The  $\text{CIII]}\lambda 1909$  line shows a more uniform distribution shifts in Pop.  $\tilde{\text{A}}$  (Fig. 7c), with a slight net shift to the red  $\sim 100 \text{ km s}^{-1}$ , smaller than the typical uncertainty in the individual shift measurements.

#### 4.1.1. Population $\tilde{\text{A}}$

Figure 7a shows that only 39 out of our 231 Pop.  $\tilde{\text{A}}$  objects have  $\text{AlIII}$  blueshifts larger than the uncertainty limit (33 objects have shifts  $< -300 \text{ km s}^{-1}$ ). This trend can also be seen in Figure 8a where we plot the  $\text{AlIII}$  shift as a function of its FWHM in bins<sup>2</sup> of  $\Delta\text{FWHM}(\text{AlIII})=1000 \text{ km s}^{-1}$ . The plot shows that, on average, Pop.  $\tilde{\text{A}}$  sources (blue circles) do not present systematic shifts in  $\text{AlIII}$  that significantly affect the FWHM measurements. This behaviour confirms the reliability of the rest-frame of the  $\text{AlIII}\lambda 1860$  for sources within the A1-A2 populations. In the relations of the  $\text{AlIII}$  shift with the bolometric luminosity or Eddington ratio (Figure 8c, e) we also do not find displacements larger than the uncertainty limit. Data were divided in sub-samples of  $\Delta\log L_{\text{bol}}=0.2 \text{ dex}$  and  $\Delta R_{\text{Edd}}=0.5$ .

Regarding the behaviour of  $\text{CIII]}$  in Pop.  $\tilde{\text{A}}$  sources, in Figure 7b we find 11 objects ( $\sim 4\%$ ) that show blueshifts larger than  $-300 \text{ km s}^{-1}$ . As observed for  $\text{AlIII}$  relations, in  $\text{CIII]}$ , we do not see clear tendencies of  $L_{\text{bol}}$  and  $R_{\text{Edd}}(\text{CIII]})$  with the shift (Fig. 8d,f), although  $\sim 17\%$  Pop. A sources shows a displacement as large as

$\sim +300 \text{ km s}^{-1}$  (52 objects, Figure 7c). This displacement toward the red is most likely due to the effect of the strong  $\text{FeII}$  emission heavily blended with  $\text{CIII]}$ .

#### 4.1.2. Extreme Population A

The spectral fitting of our 11 xA objects are shown in Figure A.1 of Appendix A. Figures 8(a,c), present our xA sub-sample in magenta points which show  $\text{AlIII}\lambda 1860$  blueshifts reaching several hundred  $\text{km s}^{-1}$ . However, those shifts are much lower than those found in  $\text{CIV}\lambda 1549$  (e.g., Sulentic et al. 2007; Section 5.3). Nine out of 11 xA sources of Figure 8c show a blueshift in  $\text{AlIII}$ , with a median shift of  $\sim -340 \text{ km s}^{-1}$  and a maximum of  $\sim -1000 \text{ km s}^{-1}$ . The Figure reveals that there is no dependence on luminosity for the  $\text{AlIII}$  shift. Figure 8e shows that not only a blueshift is detected for xA sources but that the blueshift is also significant,  $\sim 10\%$  of the FWHM. In the other hand, we note that 50 Pop. A objects ( $\sim 17\%$  of the sample) have  $R_{\text{Edd}}$  higher than the one of xA sources. As described in Sec. 3.3 and discussed in Section 5.1, we expect a higher  $R_{\text{Edd}}$  for xA objects).

$\text{CIII]}\lambda 1909$  shifts in Pop. xA sources seem to be slightly redshifted (the median shift is  $50 \pm 120 \text{ km s}^{-1}$ ), so we do not take them into account for the analysis. A redshift of  $\sim 300 \text{ km s}^{-1}$  was found in three xA spectra where  $\text{CIII]}$  is weak and is also affected by the  $\text{FeII}$  emission at  $\approx 1915 - 1920 \text{ \AA}$ .

#### 4.1.3. Population B

Our Pop. B sample is represented by red squares in Fig. 8. In general, the Pop. B  $\text{AlIII}$  profile show small displacements from the rest frame wavelength within the uncertainty limit. Figure 8a shows that the shift distribution is symmetric around 0. Figures 8c,e are consistent with this trend: symmetric displacements around 0 shift, and no dependency on the bolometric luminosity and Eddington ratio obtained with  $\text{AlIII}$ .

In Fig. 8b we observe a peak in the  $\text{CIII]}$  shift with a median value of  $160 \pm 90 \text{ km s}^{-1}$ . As seen in Fig. 5, this small redshift could indicate that sources above the  $4000 \text{ km s}^{-1}$  limit tends to “cover” the VBC spectral range. This behaviour has also been observed for the LIL  $\text{H}\beta$  line (Zamfir et al. 2010). From Figure 8d,f we observe a consistent behaviour for both  $\text{CIII]}$  and  $\text{AlIII}$ : there is no significant dependency on  $L_{\text{bol}}$  and  $R_{\text{Edd}}$ .

## 4.2. Line widths

### 4.2.1. Population $\tilde{\text{A}}$

From our spectral fitting, 111 Pop A objects (excluding the 11 xA sources) have FWHM of  $\text{CIII]}$  and  $\text{AlIII}$  not forced to be equal. We call them Pop.  $\tilde{\text{A}}^*$ . In Figure 9 we show Pop.  $\tilde{\text{A}}^*$  quasars in blue and xA quasars as magenta points. The grey line indicates the 1:1 relation, the black line is the best fit for the Pop.  $\tilde{\text{A}}^*$  sources. Using the least-square method it yields the equation:  $\text{FWHM}(\text{CIII])} \approx (663 \pm 348) + (0.709 \pm 0.061) \text{FWHM}(\text{AlIII})$ . The  $\text{AlIII}$  FWHM median value is  $3550 \pm 230 \text{ km s}^{-1}$ . The orange line is set at  $\text{FWHM}(\text{CIII])} = 0.9 \text{FWHM}(\text{AlIII})$ , according to the findings of Marziani et al. (2022, hereafter M22). The value that relates the FWHM of  $\text{CIII]}$  and  $\text{AlIII}$  should be in the range 0.8 – 1.1 for Pop A1-A2 sources. Indeed, as seen in Fig. 9 we have three objects with  $\text{FWHM}(\text{CIII]}) \sim 1.1 \text{FWHM}(\text{AlIII}\lambda 1860)$ . This behaviour indicates that A1-A2 lines are narrower than  $\text{H}\beta$  by  $\approx 10\%$ .

<sup>2</sup> Throughout Figure 8, we report the median values for each bin.



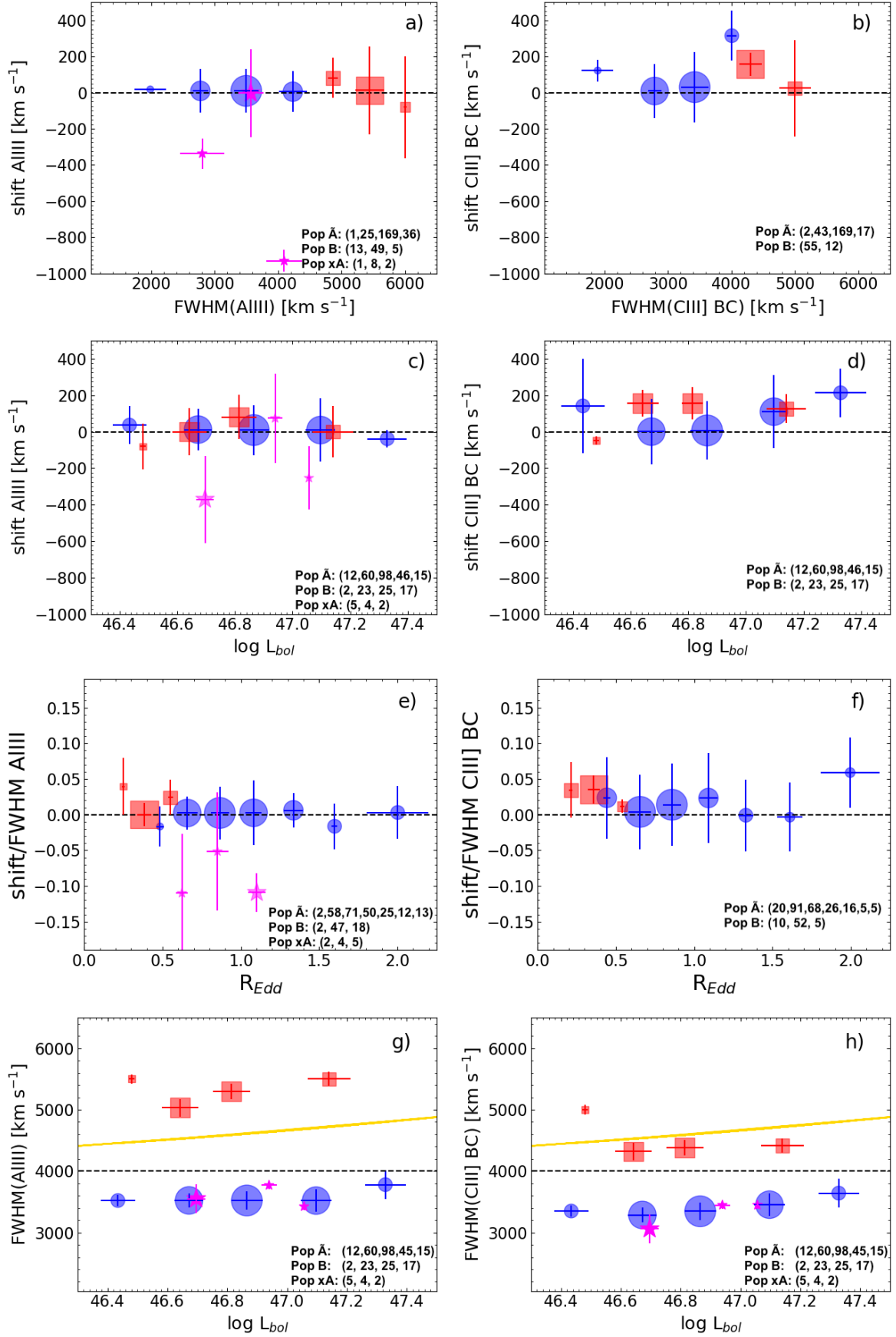


Fig. 8: Behaviour of Al $\lambda$ 1860 (left) and C $\lambda$ 1909 (right) by population. **a,b**: shift with respect to rest-frame vs. FWHM. **c,d**: shift vs.  $\log L_{bol}$ . **e,f**: ratio of shift over FWHM vs.  $R_{Edd}$ . **g,h**: FWHM vs.  $\log L_{bol}$ . Lines are the luminosity-dependent limit between Pop. A and B. of [Sulentic et al. \(2017, gold\)](#) and the empirical separation of [Sulentic et al. \(2000c, dashed\)](#). Colour-coding: Pop. A (blue circles), Pop. xA (magenta stars) and Pop. B (red squares). Reported values are sub-sample medians, error bars are 1-sigma IQRs. Marker sizes are as indicated in the legend of each plot.

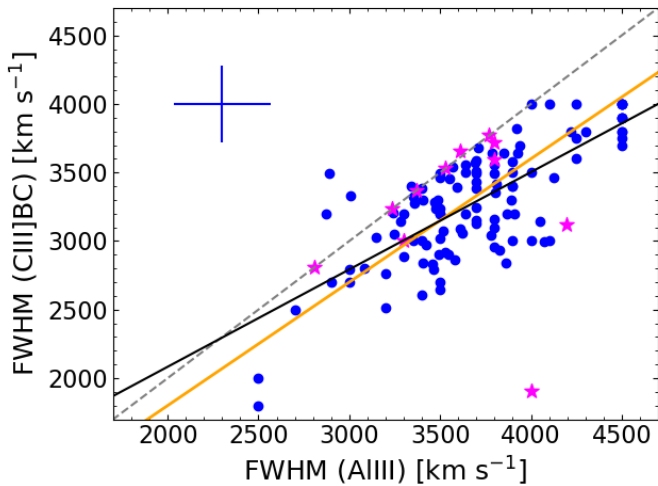


Fig. 9: FWHM( $\text{AlIII}\lambda 1860$ ) vs. FWHM( $\text{CIII]}\lambda 1909$ ) for Pop.  $\tilde{\text{A}}^*$  [FWHM( $\text{CIII]}) \neq \text{FWHM}(\text{AlIII})$ ] sources. The dots are colour-coded as Figures above by population. The dashed line traces the 1:1 relation; the black line is the best fit obtained using the least-square method and the orange one is the line of  $\text{FWHM}(\text{CIII]}) = 0.9 \text{FWHM}(\text{AlIII})$ . The cross shows sIQRs of the uncertainties.

#### 4.2.2. Extreme Population A

The physical reason to use the ratio of the shift from the central wavelength over the FWHM in Figure 8e,f resides in the effect of outflow motions on the BC. An outflow component leads to an increase in the profile width (as seen for  $\text{CIV}\lambda 1549$  and  $\text{MgII}\lambda 2800$ , e.g., [Marziani et al. 2016, 2013](#); [Denney 2012](#); [McLure & Jarvis 2002](#)). The decomposition of the  $\text{xA AlIII}\lambda 1860$  profiles shown in Appendix A validates this assumption. In our  $\text{xA}$  sub sample, SDSS J003546.29-034118.2 is the source with the highest blueshift,  $-1010 \pm 80 \text{ km s}^{-1}$ , that is as well the quasar with the largest  $\text{FWHM}(\text{AlIII}) = 4200 \pm 340 \text{ km s}^{-1}$ . Another example is SDSS J152314.49+375928.9, with a shift of  $-850 \pm 30 \text{ km s}^{-1}$ , and a  $\text{FWHM}(\text{AlIII}) = 4000 \pm 400 \text{ km s}^{-1}$ . The other 9  $\text{xA AlIII}$  profiles show shifts between  $-500$  and  $270 \text{ km s}^{-1}$  with  $\text{FWHM}(\text{AlIII})$  between  $2500$  and  $4000 \text{ km s}^{-1}$ . In the  $\text{AlIII}$  case (Fig. 8e), the largest ratio of shift/FWHM is  $\lesssim -0.15$  which implies that the broadening effect might significantly affect the  $\text{AlIII}$  line width.

#### 4.2.3. Population B

The highest value of  $\text{AlIII}$  FWHM observed in Pop. B objects is  $6500 \text{ km s}^{-1}$ . Only one object shows a FWHM of  $4000 \text{ km s}^{-1}$ , indicating that the  $\text{AlIII}$  line is broader than in Pop. A spectra but not as wide as the  $\text{CIII] VBC}$ . The median values are  $\text{FWHM}(\text{CIII] BC}) = 5300 \pm 250 \text{ km s}^{-1}$  and  $\text{FWHM}(\text{CIII] VBC}) = 8124 \pm 410 \text{ km s}^{-1}$ . The inclusion of a VBC of  $\text{CIII]}$  in the red side of the Pop. B spectra is evident as seen in Figure 5. In Pop. B objects we do not expect strong contribution of  $\text{FeIII}$ , so the residual seen in the fit with no VCB (Fig. 5, upper panel) should be also part of  $\text{CIII]}$ .

The case of a VBC in  $\text{AlIII}$  and  $\text{SiIII]$  is not so evident. It could be that for  $\text{AlIII}$  and  $\text{SiIII]$  it is also necessary to add a VBC due to the large FWHM observed (up to  $\sim 6500 \text{ km s}^{-1}$  for  $\text{AlIII}$  and  $5800 \text{ km s}^{-1}$  for  $\text{SiIII]$ ). In the case of  $\text{AlIII}$ , the blending is not extremely severe, so we are able to efficiently deblend the BC (as seen in Figure 3). The blend profile suggests that if  $\text{AlIII}$

VBC is present, it might be very weak, probably unresolved and not dominant in the emission line profile. A VBC might not be detected and lost in the spectral noise.

In Section 5.4 we derive constraints on the  $\text{AlIII}$  and  $\text{SiIII]$  VBC.

## 5. Discussion

The  $M_{\text{BH}}$  computations are closely related to the FWHM of prominent broad components and the underlying continuum. Therefore, the decomposition of the line profile becomes important to isolate the virialized component from other components, either coming from an outflow (blueshifted) or possibly coming from an inflow region (redshifted, [Wang et al. 2017](#)). We explore different  $M_{\text{BH}}$  estimators (Sections 5.1 and 5.2) not as affected by shifts as  $\text{CIV}\lambda 1549$  (Sect. 5.3). For Pop. B objects, we analyse the possibility of a VBC in  $\text{AlIII}$  and  $\text{SiIII]$  (Section 5.4).

### 5.1. Virial mass and Eddington ratio estimates with $\text{AlIII}\lambda 1860$

Using the FWHM of two prominent lines of the  $1900\text{\AA}$  blend,  $\text{AlIII}$  and  $\text{CIII]$ , we compute the virial  $M_{\text{BH}}$  with two methods: (1) [M22](#) (equations 3-4) derived from the comparison of the FWHM of  $\text{H}\beta$  with  $\text{AlIII}$  and  $\text{CIII]$ ; (2) [Vestergaard & Peterson \(2006, hereafter VP06, Equations 5 and 7\)](#) that are based on the  $\text{H}\beta$  and  $\text{CIV}\lambda 1549$  line widths.

The [M22](#) scaling laws take the form:

$$\log M_{\text{BH}}(\text{AlIII}) \approx (0.580_{-0.040}^{+0.035}) \log L_{1700,44} + 2 \log(\xi_{\text{AlIII}} \text{FWHM}(\text{AlIII})) + (0.51_{-0.05}^{+0.05}) \quad (3)$$

$$\log M_{\text{BH}}(\text{CIII])} \approx (0.645_{-0.045}^{+0.045}) \log L_{1700,44} + 2 \log(\xi_{\text{CIII])} \text{FWHM}(\text{CIII]))} + (0.355_{-0.045}^{+0.075}). \quad (4)$$

Here  $\xi$  is a correction needed in the FWHM (Section 4.2.1), for  $\xi_{\text{AlIII}} \approx 1$  and  $\xi_{\text{CIII])} \approx 1.25$ .

[VP06](#) use the optical continuum luminosity  $L_{\lambda}(5100\text{\AA})$  along with  $\text{FWHM}(\text{H}\beta_{\text{BC}})$  and the UV continuum  $L_{\lambda}(1350\text{\AA})$  along with  $\text{FWHM}(\text{CIV}\lambda 1549_{\text{BC}})$ . Considering the different continuum windows of these equations, we found it necessary to extrapolate the continuum obtained from `specfit` to a wavelength as close as possible to  $5100 \text{\AA}$  or  $1350 \text{\AA}$ . We applied the ‘‘surrogate’’ lines  $\text{AlIII}\lambda 1860$  and  $\text{CIII]}\lambda 1909$  in both equations of [VP06](#). This means that we can directly compare the  $M_{\text{BH}}(\text{AlIII})$  and  $M_{\text{BH}}(\text{CIII])}$  from the scaling relations of [M22](#) to the ones of [VP06](#) using  $\text{FWHM AlIII}\lambda 1860$  or  $\text{CIII]}\lambda 1909$  in place of  $\text{FWHM CIV}\lambda 1549$  or  $\text{H}\beta$ .

The comparison of  $M_{\text{BH}}$  from equations 3 and 4 is presented in Figure 10 along with the residuals of each set with  $\delta \log M_{\text{BH}} = \log M_{\text{BH}}(\text{AlIII}) - \log M_{\text{BH}}(\text{CIII])}$ . In the Figure, the grey line indicates the 1:1 relation, and the black line is the best fit for the Pop.  $\tilde{\text{A}}^*$  sources using the least-square method. For the [M22](#) results (Figure 10a) the equation is  $\log M_{\text{BH}}(\text{CIII])} \approx (-1.017 \pm 0.095) + (1.131 \pm 0.085) \log M_{\text{BH}}(\text{AlIII})$ ; the rms of the linear fit is 0.043 and the deviation from the 1:1 relation is 0.14. In the other two panels of Figure 10, we used Eq. 7 of [VP06](#) by replacing the FWHM of  $\text{CIV}$  with the FWHM of  $\text{AlIII}$  and  $\text{CIII]$ . Figure 10b shows the relation for  $M_{\text{BH}}(\text{AlIII})$  using Eq. 3 vs.

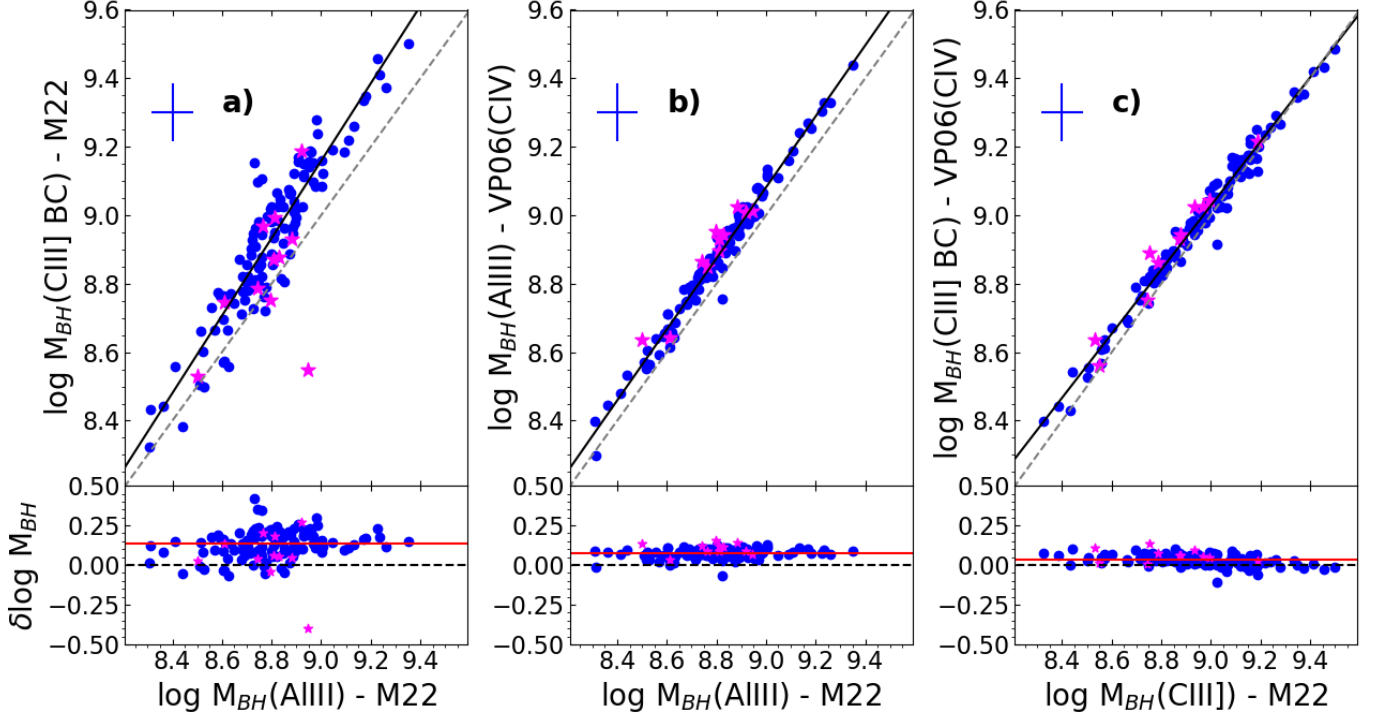


Fig. 10: *Upper panels*: Log space of  $M_{\text{BH}}(\text{AlIII})$  vs.  $M_{\text{BH}}(\text{CIII})$  computed with the scale relations of **M22** and **VP06** for the Pop.  $\text{A}^*$  sources [ $\text{FWHM}(\text{CIII}) \neq \text{FWHM}(\text{AlIII})$ ]: a)  $\log M_{\text{BH}}(\text{AlIII})$  vs.  $\log M_{\text{BH}}(\text{CIII})$  both using **M22** SR; b)  $\log M_{\text{BH}}(\text{AlIII})$  using Eq. 3 by **M22** vs. Eq. 7 by **VP06**; c)  $\log M_{\text{BH}}(\text{CIII})$  using Eq. 4 by **M22** vs. Eq. 7 by **VP06**. *Lower panels*: Residuals of each  $M_{\text{BH}}$  computation,  $\delta \log M_{\text{BH}}$ . Colour-code as Figure 9. Dashed line traces the 1:1 relation; the filled line is the best fit obtained using the least-square method and the red line is the median value of  $\delta \log M_{\text{BH}}$ . The uncertainties of the Pop.  $\text{A}^*$  sample are marked with a cross and calculated as the sIQR.

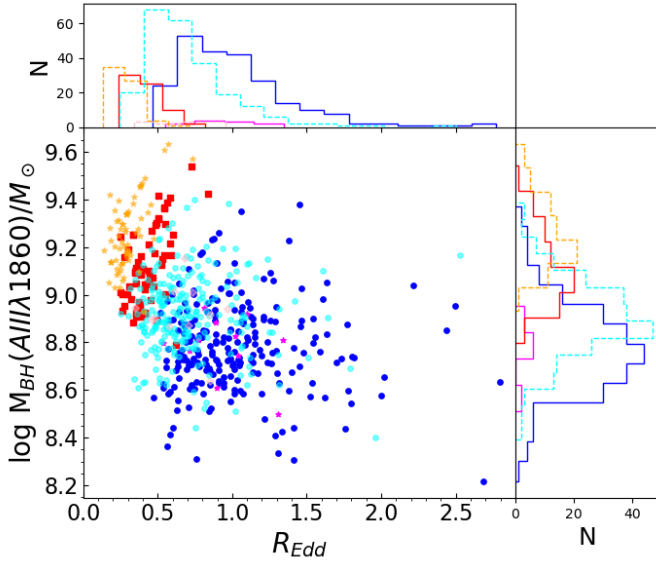


Fig. 11: Distribution of  $\log M_{\text{BH}}(\text{AlIII}\lambda 1860)$  vs.  $R_{\text{Edd}}$ . Colour-code is as follows: the scale relations of **M22** in blue, red and magenta and for the one of **VP06** (Equation 5) in light blue, orange and light magenta for Pops.  $\text{A}$ ,  $\text{B}$  and  $\text{xA}$ , respectively.

**VP06** Eq. 7. There is very good agreement between the estimations:  $\log M_{\text{BH}}(\text{AlIII})_{\text{M22}} \approx (-0.249 \pm 0.045) + (1.037 \pm 0.065) \log M_{\text{BH}}(\text{AlIII})_{\text{VP06}}$  with a Pearson correlation of 0.98; the stan-

dard error (STD err) of the linear fit is 0.015 and the deviation from the 1:1 relation is 0.08. Figure 10c displays the relation of  $M_{\text{BH}}(\text{CIII})$  using Eq. 4 vs. **VP06** Eq. 7. In this case, we also observe a good agreement between each estimation. The resultant equation is  $\log M_{\text{BH}}(\text{CIII})_{\text{M22}} \approx (0.609 \pm 0.085) + (0.935 \pm 0.065) \log M_{\text{BH}}(\text{CIII})_{\text{VP06}}$  with a Pearson correlation of 0.99; the STD err of the linear fit is 0.012 and the deviation from the 1:1 relation is 0.04. The scatter of Figure 10b,c is smaller than in Figure 10a due to fact that the equations of **M22** are based on **VP06**.

As for the case of Eq. 5 of **VP06** by replacing the FWHM of  $\text{H}\beta$  for the FWHM of  $\text{AlIII}$  and  $\text{CIII}$ , we observed a discrepancy between estimations, a much larger scatter and systematic changes associated probably to the extrapolation of the continuum from  $\approx 4000\text{\AA}$  to  $5100\text{\AA}$ . We see a similar situation for  $\text{AlIII}$  and  $\text{CIII}$  for both comparisons, both of them with a Pearson correlation of  $\sim 0.8$  and a resultant equation of  $\log M_{\text{BH}}(\text{AlIII}, \text{CIII})_{\text{M22}} \approx 0.6 \log M_{\text{BH}}(\text{AlIII}, \text{CIII})_{\text{VP06}}$ . These findings proves that  $\text{AlIII}$  and  $\text{CIII}$  are equivalent as virial broadening estimators for quasars (with a Pearson correlation coefficient of 0.93 for **M22**) at intermediate  $z$  from observations obtained from large surveys such as the SDSS.

In HILs such as  $\text{CIV}\lambda 1549$ , the contamination of an outflow introduces a bias in the black hole mass estimations (see Sec. 5.3), because of over-broadening of the lines. The dynamic associated with a virialized system is different from the outflow that emerges from a system dominated by radiation pressure. A similar effect could be seen in the IIL  $\text{AlIII}$  for  $\text{xA}$  objects, but the contribution of the outflow is much lower than in the case of  $\text{CIV}\lambda 1549$ . This accounts for the good agreement found between

the scaling laws for C<sub>IV</sub>λ1549 by VP06 and the one of M22. The C<sub>IV</sub>λ1549 scaling law of VP06 was built around the assumption that the C<sub>IV</sub>λ1549 FWHM was as good as Hβ for virial mass estimation. Using the C<sub>III</sub>λ1909 (or Al<sub>III</sub>λ1860), we use a line that is truly equivalent to Hβ (M22) and is not strongly affected by any non-virial component.

Several authors proposed that the Eddington ratio is driving the E1 MS (Marziani et al. 2001, 2003b; Shen & Ho 2014; Sun & Shen 2015). Trends in  $R_{\text{Edd}}$  are also reflected in the X-ray properties (Boller et al. 1996; Wang et al. 1996; Laor et al. 1997), C<sub>IV</sub>λ1549 line profiles (Wills et al. 1999; Sulentic et al. 2000c, 2007), and in virial BH mass estimates using the width of the broad emission lines (Laor 2000; Boroson 2002; Dong et al. 2011). The distribution of  $M_{\text{BH}}(\text{AlIII})$  vs  $R_{\text{Edd}}$  is shown in Figure 11. Eddington luminosities have been calculated based on masses obtained from the FWHM(Al<sub>III</sub>λ1860) following the relation:  $L_{\text{Edd}} \approx 1.5 \times 10^{38} (M_{\text{BH}}/M_{\odot}) [\text{erg s}^{-1}]$  (e.g., Netzer & Marziani 2010; Netzer 2015). The bolometric correction for  $L_{\lambda}$  (1700Å), 6.3 was taken from MS14, and from Richards et al. (2006) the ones for 1350Å (5.75) and for 5100Å (10.3).

Fig. 11 shows that Pops. B and  $\tilde{A}$  appear to be segregated mainly on the basis of  $R_{\text{Edd}}$ : few Pop. B sources are in excess of  $R_{\text{Edd}} \approx 0.5$ . The wide majority of Pop.  $\tilde{A}$  is constrained in the range  $0.4 \lesssim R_{\text{Edd}} \lesssim 1.2$ . A minority of data points scatter in the range  $1.2 \lesssim R_{\text{Edd}} \lesssim 3$ . If orientation plays a role, and if pole-on orientation leads to narrower lines (McLure & Jarvis 2002; Collin et al. 2006; Decarli et al. 2011; Mejía-Restrepo et al. 2017, 2018), the  $M_{\text{BH}}$  might be severely underestimate and  $R_{\text{Edd}}$  overestimated. A similar effect has been already seen in the  $M_{\text{BH}}$  vs. luminosity diagram (e.g., Marziani et al. 2006).

We also analysed the parameter space of the UV diagnostic ratios vs.  $R_{\text{Edd}}$  plane for the Pop.  $\tilde{A}$  sources, however, we found no strong correlations (Figure 12). Table 1 reports the median values of the line ratios. The condition  $\text{CIII}\lambda 1909/\text{SiIII}\lambda 1892 \leq 1$  seems to be sufficient to identify xA quasars. Yet, xA quasars are not associated with the highest  $R_{\text{Edd}}$  (see also Figure 11). This might be a consequence of an overbroadening due to an outflow component, increasing  $M_{\text{BH}}$  for xA sources and therefore lowering  $R_{\text{Edd}}$ . The median excess in the virial luminosity (rose bars in Fig. 13) suggests a median  $M_{\text{BH}}$  overestimate  $\delta \log M_{\text{BH}} \approx 0.2$ . Pop.  $\tilde{A}$  sources with  $R_{\text{Edd}} \gtrsim 2$  might be oriented preferentially pole-on, leading to a strong underestimate of the black hole mass and hence to an overestimate of the Eddington ratio (as observed in Figure 11, the  $R_{\text{Edd}}$  is up to  $\sim 2.5$ ).

## 5.2. Virial luminosities and outflow broadening

The physical parameters of xA quasars are correspondingly extreme, with maximum radiative output per unit of mass close to their Eddington limit. This condition is predicted by accretion disk theory at high accretion rates: radiative efficiency low and Eddington ratio saturating towards a limiting value (Mineshige et al. 2000; Sądowski 2011; Sądowski et al. 2014, and references therein). We also expect that the intensity ratios of the intermediate and low ionisation lines in xA quasars remain almost the same: only the line width increases with luminosity (Negrete et al. 2012, 2013). The spectral invariance with luminosity implies that the radius of the emitting regions should rigorously scale as  $L^{1/2}$ ; if not, the ionisation parameter  $U$  should change with luminosity (Marziani et al. 2021). Putting together these considerations: (1)  $L/L_{\text{Edd}} = \text{const.}$ , (2)  $r \propto L^{1/2}$ , together with (3) the definition of Eq. 1  $M_{\text{BH}} \propto r \text{FWHM}^2$ , we obtain a re-

lation linking luminosity and line width, known as the “virial luminosity equation” (MS14):

$$L_{\text{Vir}} = L_0 \cdot (\text{FWHM})_{1000}^4 \text{ erg s}^{-1} \quad (5)$$

where  $L_0 = 7.88 \times 10^{44}$  and the FWHM is of the virialized BC in units of  $1000 \text{ km s}^{-1}$  (see eq. 6 in MS14 for the complete derivation). The FWHM of Al<sub>III</sub> is the adopted virial broadening estimator for our work. We calculated  $L_{\text{Vir}}$  for the 11 xA sources and the average and median values are reported in Table 1. However, there are two effects that can significantly affect the luminosity estimations: an outflow that broadens the virial component, and an orientation effect that narrows it.

For xA sources, the Al<sub>III</sub> shift/FWHM ratio can be up to  $\sim -0.1$  (Fig. 8,e). The dominant effect on our sources may be due to an outflow since the virial luminosities are larger than the cosmological ones. We have 11 extreme sources, of which six objects have  $\delta \log L = \log L_{\text{bol}} - \log L_{\text{Vir}} \approx -0.2$  (magenta bars in Figure 13). SDSS J003546.29, J152314.49 and J023055.54 showed a difference between the cosmological and virial luminosities under -0.2 and are sources with an Al<sub>III</sub> blueshift. SDSS J003546.29 having a  $\delta \log L = -0.75$  and shift Al<sub>III</sub>  $\approx -1000 \text{ km s}^{-1}$ .

## 5.3. C<sub>IV</sub>λ1549 and Al<sub>III</sub>λ1860 inter-comparison

The blueshift of C<sub>IV</sub>λ1549 is usually evidence of strong outflows (e.g. Richards et al. 2011) that, most likely, results from the presence of a radiation line-driven accretion-disc wind (Gallagher et al. 2015 and references therein). Therefore, a prominent blue component over the line profile is expected, especially at high/intermediate redshift (Martínez-Aldama et al. 2018). However, when compared to samples with lower redshift, Pop. A sources at intermediate redshifts tend to show broader and more blueshifted components of C<sub>IV</sub>. They are indicative of wind activities surrounding the central region (Deconto-Machado et al. 2021). Therefore, black hole masses based on the FWHM(C<sub>IV</sub>) emission line can be overestimated by a factor of 4-5 at large blueshifts and are biased due to this non-virial component (Coatman et al. 2016; Denney 2012).

A sub-sample from Shen et al. (2011) was extracted to compare the C<sub>IV</sub>λ1549 profile with our Al<sub>III</sub> sample. The criteria used were: luminosity distribution consistent with the one of the Al<sub>III</sub>λ1860 sample. The results are shown in Fig. 14, for the FWHM and peak shift of the line. The blue lines show the distribution of bootstrap replications of the bolometric luminosity distribution, for 300 objects pooled out of  $\sim 50,000$  sources from the Shen et al. (2011) catalogue. The luminosity distributions of the bootstrapped samples overlay the one of the present samples since the source from Shen et al. (2011) where pooled preserving the relative prevalence of the Al<sub>III</sub>λ1860 luminosity been (shaded histogram in Fig. 14). For both C<sub>IV</sub>λ1549 FWHM and shift, the distribution imply extremely high probabilities that they are not consistent. In particular, the FWHM C<sub>IV</sub>λ1549 appears to be systematically broader than the one of Al<sub>III</sub> by  $\approx 1500 \text{ km s}^{-1}$ . While the Al<sub>III</sub> blueshifts are modest (within  $|\delta v_r| \lesssim 500 \text{ km s}^{-1}$ , and the distribution appears centred at rest frame and only slightly skewed to the blue, the C<sub>IV</sub>λ1549 line presents a systematic blueshift by  $\approx -600 \text{ km s}^{-1}$ .

The C<sub>IV</sub>λ1549 shift has been analysed with respect to Hβ (e.g., Leighly & Moore 2004; Marziani et al. 2010; Sulentic et al. 2017; Vietri et al. 2018), and interpreted as a strong wind contribution affecting the C<sub>IV</sub>λ1549 profile in the form of an excess

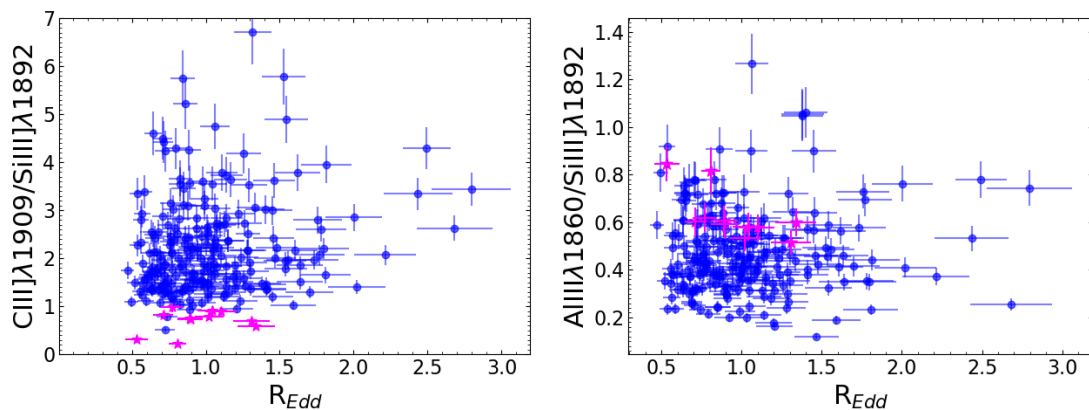


Fig. 12: Distribution of the UV diagnostic ratios of MS14: AlIII]λ1860/SIII]λ1892 (left) and CIII]λ1909/SIII]λ1892 (right) with respect  $R_{Edd}$  (AlIII), for Pop.  $\tilde{A}$  and xA sources only

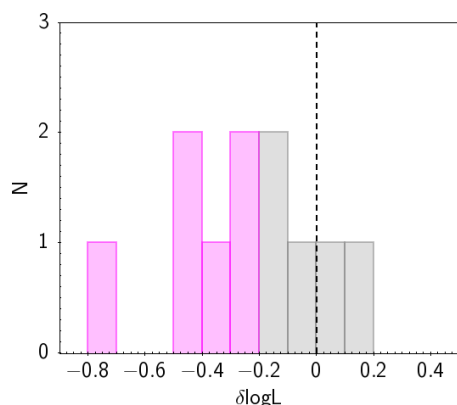


Fig. 13: Distribution of the luminosity difference between concordance cosmology determinations and virial ones,  $\delta \log L$ . Colour-code: Grey bars are the 5 objects that lie under our uncertainties of  $\delta \log L$  and the 6 objects in magenta are the ones that shows an outflow effect ( $\delta \log L \lesssim -0.2$ ).

blueshifted emission. The same difference has been revealed in a detailed same-source, inter-line comparison between AlIII and CIII]λ1549 in  $\approx 20$  xA sources (Martínez-Aldama et al. 2018). Fig. 14 provides a statistical confirmation that the CIII]λ1549 blueshifted emission is broadening and shifting considerably the CIII]λ1549 profile with respect to the one of AlIII]λ1860.

#### 5.4. A model for the Population B CIII]λ1909 profile

Is our model of the 1900 blend adequate? This work has convincingly shown the need to include a VBC to account for the CIII]λ1909 profile. Even if the SIII]λ1892 is heavily blended, the fits detect an emission peak between AlIII and CIII]λ1909, implying that the SIII]λ1892 core component is always prominent. There is no doubt about the existence of a core component (i.e., the BC) for AlIII. However AlIII is the weakest line in the blend, and some VBC emission could be lost in noise.

We can analyse the expectation of VBC emission considering that (1) the velocity field of the emitting regions is predominantly virial in Pop. B sources, as established by early reverberation mapping studies (Peterson & Wandel 1999, 2000), and that (2) the VBC is a heuristic representation of the innermost part of the BLR. This VBC could be physically associated to inflowing gas (Wang et al. 2017; Giustini & Proga 2019) or due to an

effect of the gravitational redshift (Netzer 1977; Zheng & Sulentic 1990; Corbin 1995; Liu et al. 2017; Mediavilla et al. 2018). This component has been observed in sources with masses in the range  $10^8$ – $10^{10} M_{\odot}$  (Bon et al. 2015), comparable to the Pop. B mass values of the present sample, with mean  $\log M_{BH} = 9.1 [M_{\odot}]$ .

In this way, three empirical approaches are in order: (1) a fit with only the BCs (M1); (2) a fit in which one VBC is assumed for CIII]λ1909 only (as done for all Pop. B sources, M2); (3) a fit in which 3BCs and 3VBCs are introduced, with restriction on consistent shifts and widths for the BCs and VBCs (M3) as seen in Figure 15a. This last option implies 8 free parameters (peak shifts and wavelengths are locked). It is probably the most appropriate in physical terms, but is very difficult to implement for individual sources. The three fits were carried out on an average composite for all Pop. B sources, and the resulting ratios are reported for the three models in Table 2. The basic inference is that the BC ratios AlIII]λ1860/SIII]λ1892 and SIII]λ1892/CIII]λ1909 remain consistent if different models are assumed. A second result is that the VBC/BC ratio is  $<1$  and  $\ll 1$  for SIII]λ1892 and AlIII]λ1860, respectively.

The physical implications for the line emitting regions have been analysed using CLOUDY 17.02 (Ferland et al. 2017) arrays of photoionisation simulations computed for an unrelated work (Śniegowska et al. 2021). Briefly, they assumed a standard AGN continuum implemented in CLOUDY, solar metallicity, canonical value of the Hydrogen column density ( $10^{23} \text{ cm}^{-2}$ ), no micro-turbulence. They were computed for an array of ionisation parameter and density covering the ranges (in log)  $-4.5 - 1$ , and  $7 - 14 [\text{cm}^{-3}]$ , respectively.

Fig. 16 shows the behaviour of the ratios AlIII]λ1860/SIII]λ1892, SIII]λ1892/CIII]λ1909 and AlIII]λ1860/CIII]λ1909 as a function of ionisation parameter and hydrogen density. The typical ratios measured on the Pop. B sample and on the composite spectrum indicate that the BC is emitted in a region of moderate density and high ionisation ( $U \sim 10^{-1}$ ,  $n_H \sim 10^{11} \text{ cm}^{-3}$ ). Similar values are found for the VBC.

To push the analysis one step forward we consider the ratios estimated for Model 4 (a synthetic model with VBC and BC for the three lines, Table 2) as seen in Figure 15b. This model was made using M3 flux values as an initial condition, then let the model adapt to the better statistical values (along very well defined physical ranges) varying the fit with a million random iterations. The significance of  $\chi^2$  variations is described by F

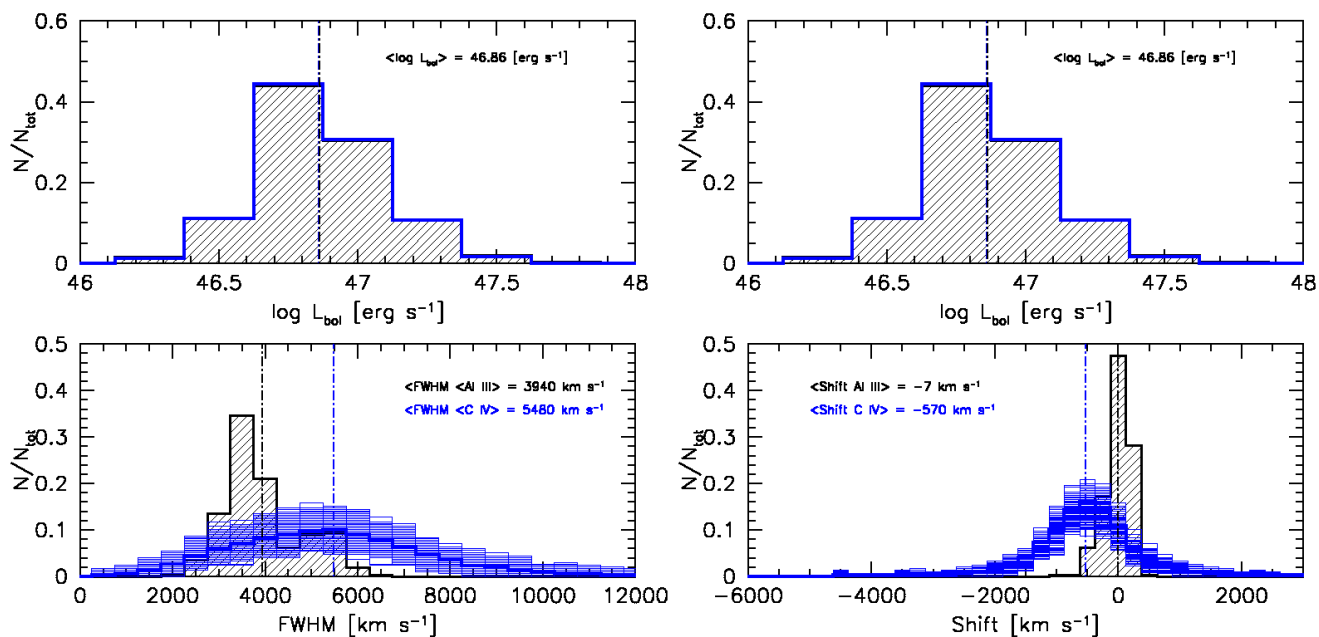


Fig. 14: *Left*: inter-comparison between the Al III  $\lambda$ 1860 of the present sample (hatched histograms) and the C IV  $\lambda$ 1549 FWHM distribution of the sample of Shen et al. (2011), for matching luminosity distributions (top panel). The bottom panel thin blue lines show the binned distributions of bootstrap replications of the Shen et al. (2011) data; the thick blue line is their average. *Right*: same for peak shift.

statistics appropriate for ratios of  $\chi^2$  values (Bevington & Robinson 2003),  $F = \chi_v^2 / \chi_{v,min}^2$ , with degrees of freedom  $v \approx 165$ .  $F \approx 1.30$  provides  $2\sigma$  confidence ranges on the parameters. The final fluxes obtained for the M4 BC and VBC fluxes are the ones that satisfies  $F$  within a  $2\sigma$  confidence level ( $F(2\sigma)$ , Figure 15b). In the Figure 15b we can see the distributions in light-dark red, green and blue for Al III, Si III and C III BC - VBC, respectively. The dotted line of each distribution are the median values used in the UV ratios in Table 2. Our synthetic models that satisfied the condition of the  $F(2\sigma)$  showed Gaussian distributions for the BC and VBC fluxes centred in one very well defined value, except for Si III VBC (Figure 15c,d). The median values are marked for each distribution and corresponds to the dotted black lines of Figure 15b.

Fig. 17 shows the regions in the parameter plane that are consistent with the ratios built from the three lines in the blend. For the BC there is a very well defined  $(U, n_H)$  region where the three ratios cross; it means that in this region the values of  $(U, n_H)$  are able to reproduce the observed ratios:  $\log U \sim -1.00^{+0.12}_{-0.28}$ ,  $\log n_H \sim 10.78^{+0.28}_{-0.08} \text{ cm}^{-3}$ . Similar values are derived if the BC and VBC are added together:  $\log U \sim -1.03^{+0.31}_{-0.19}$ ,  $\log n_H \sim 10.72^{+0.19}_{-0.15} \text{ cm}^{-3}$ , where the uncertainty range has been set from the  $\pm 1\sigma$  uncertainties for the individual line ratios. These values indicate moderate density and fairly high ionisation as expected for Population B sources (Negrete et al. 2013, 2014). We warn that our single zone model is certainly not adequate to represent the complexity of the emitting region. In the case of Pop. B, there is a most likely a range of densities, column densities, and ionisation parameters that makes the locally-optimised cloud model (Baldwin et al. 1995; Korista et al. 1997b) the most appropriate.

The case of the VBC deserves special attention. We are dealing with emission that is well-constrained only in the case of C III  $\lambda$ 1909, and that is presumably much weaker than the corresponding BC emission for Al III  $\lambda$ 1860 and Si III  $\lambda$ 1892. Using

the ratios of the best fit to the synthetic spectrum we obtain  $\log U \sim -0.72^{+0.27}_{-1.53}$ ,  $\log n_H \sim 10.27^{+0.19}_{-0.19} \text{ cm}^{-3}$ . Due to the very low Si III  $\lambda$ 1892/C III  $\lambda$ 1909 and Al III  $\lambda$ 1860/Si III  $\lambda$ 1892 intensity ratios derived from the fit (actually consistent with 0 within the uncertainties), the lower limit of both  $U$  and  $n_H$  are practically unconstrained.

Further clues can be obtained considering that the line width should be inversely proportional to the square root of the radius of the emitting region:  $\text{FWHM} \propto 1/r^{1/2}$ , as per Eq. 1. The BC over VBC FWHM ratio is  $\approx 0.8$ , implying that the ratio of the radii should be  $\approx 0.64$ . For constant  $n_H$ , this would imply an increase in  $\delta \log U \sim +0.38$ . The diagnostics from the blend for the VBC are very poor (a more refined analysis should involve measurements of at least C IV  $\lambda$ 1549 and He II  $\lambda$ 1640 which are not covered in the spectra of our sample). However, there is slight increase in  $U$  moving from the BLR to the VBLR that does not suggest any gross inconsistency with the virial approach.

Fig. 16 indicates that that, for a likely value of  $n_H \sim 10^{11} \text{ cm}^{-3}$ , moving from  $\log U \sim -1$  toward higher  $U$  values, we may expect a lowering of the Si III  $\lambda$ 1892/C III  $\lambda$ 1909 ratio to level that may make the VBC of Si III  $\lambda$ 1892 difficult to detect. At the same time, the Al III  $\lambda$ 1860/Si III  $\lambda$ 1892 ratio might increase sharply for  $\log U \gtrsim -0.5$ , reaching  $\approx 1$  for  $\log U \gtrsim -0.0$ . At that value of the ionisation parameter, the Al III  $\lambda$ 1860 VBC should be stronger than the one of C III  $\lambda$ 1909. The composite profile (Fig. 15) disfavours the possibility that the Al III  $\lambda$ 1860 VBC and in turn the  $U$  could be that high: in Pop. B, the intensity of Al III  $\lambda$ 1860 is lower than the one of Si III  $\lambda$ 1892 (Bachev et al. 2004; Kuraszewicz et al. 2004; Lira et al. 2017, 2018). ionisation parameter  $\log U \sim -0.25$  might be a possibility entailing Al III  $\lambda$ 1860/C III  $\lambda$ 1909  $\approx 0.3$ , Al III  $\lambda$ 1860/Si III  $\lambda$ 1892  $\approx 2$ , and Si III  $\lambda$ 1892/C III  $\lambda$ 1909  $\approx 0.15$  (assuming  $n_H = 10^{11} \text{ cm}^{-3}$ ).

In summary, these consideration justify the neglect of a Si III  $\lambda$ 1892 VBC. The possibility of an Al III  $\lambda$ 1860 VBC domi-

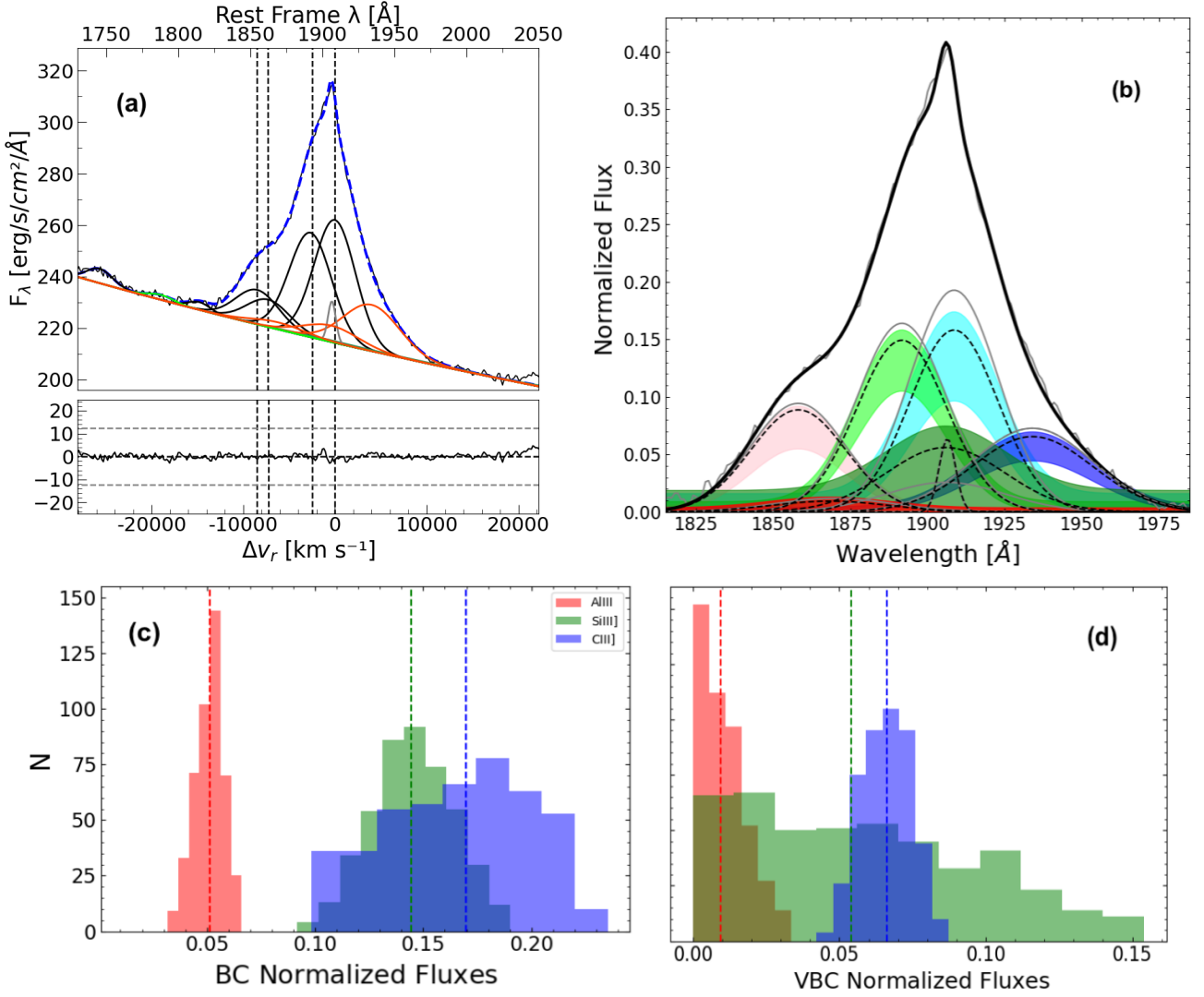


Fig. 15: *Upper left*: *specfit* model (M3) of the composite spectra of Pop. B sources with VBC (in red) added to the profile of AlIII, SiIII and CIII. Abscissa scales are rest-frame wavelength in  $\text{\AA}$ . Ordinate scale is the specific flux in units of  $10^{-17} \text{ ergs s}^{-1} \text{ cm}^{-2} \text{ \AA}^{-1}$ . *Upper right*: Synthetic model (M4) with BC+VBC in all three lines with the median value (dashed line) and their uncertainties regions of each profile in light and dark tone: red, green and blue for AlIII, SiIII and CIII BC - VBC respectively. Grey lines are the M3 flux values as the initial condition. *Lower panels*: Gaussian distributions of the BC - VBC fluxes obtained with a million random iterations of M3 with values that satisfies the condition of  $\chi^2(\text{M4})/\chi^2_{\min}(\text{M4}) < F(2\sigma)$ .

nating the AlIII1860 cannot be excluded if the ionisation parameter is high. Against this prospect goes the empirical fact that the FWHM of AlIII1860 and SiIII1892 BC are consistent.

## 6. Summary and conclusions

The present investigation has shown that the intermediate ionisation lines are little affected by outflows, and that the AlIII and CIII are equivalent (with some caveats) as virial broadening estimators for quasars, providing a suitable tool for  $M_{\text{BH}}$  estimates at intermediate  $z$  from observations obtained from a big survey such as the SDSS. More in detail, the results of the present investigation can be summarised as follows:

- We carried out a redshift correction of the sample spectra using the narrow LIL [OII] rest-frame wavelength. The rest-frame of the 1900 $\text{\AA}$  blend corrected in redshift for the [OII]

line proved the effectiveness of AlIII and CIII as rest-frame estimators.

- We subdivided the sample into Population A and B. We took into account the luminosity-dependent relation of Sulentic et al. (2017). Within Pop. A, extreme Population A have been considered separately.
- Pop. A quasars constitute 78% of the sample with 11 sources classified as extreme accretors, and 22% as Pop. B quasars out of a sample of 309 objects. We observed a bias against high Eddington ratio sources due to the absence of [OII] in the spectra, and a Malmquist-type bias at low Eddington ratio.
- Applying the *specfit* routine of IRAF, we were able to fit the most prominent emission lines of the 1900 $\text{\AA}$  blend simultaneously, proving that we can measure widths of AlIII and CIII (and SiIII) even if they are blended.
- In terms of tendencies observed for each population: Pop. A has shown no shifts in the median sub-samples from the

Table 2: UV diagnostic ratios of MS14 values obtained on an average composite for all Pop. B sources with different considerations for the AlIII, CIII] and SiIII] profile lines.

	M1	M2	M3	M4
	(a)	(b)	(c)	(d)
AlIII BC/ SiIII]BC	0.62±0.19	0.65±0.39	0.61±0.06	0.37±0.73
CIII]BC/ SiIII]BC	1.34±0.25	1.28±0.32	1.16±0.07	1.39±0.79
AlIII BC/ CIII] BC	0.46±0.14	0.51±0.28	0.53±0.08	0.27±0.78
AlIII VBC/ SiIII]VBC	-	-	0.42±0.06	0.19±3.95
CIII]VBC/ SiIII]VBC	-	-	2.87±0.07	1.65±2.23
AlIII VBC+BC/ SiIII]BC+VBC	-	-	0.58±0.12	0.32±1.10
CIII]VBC+BC/ SiIII]BC+VBC	-	-	1.45±0.14	1.46±0.90
AlIII VBC/ AlIII BC	-	-	0.15±0.03	0.17±2.45
SiIII] VBC/ SiIII] BC	-	-	0.21±0.01	0.33±2.23
CIII] VBC/ CIII] BC	-	-	0.51±0.01	0.39±0.79
$\chi^2$	0.11994	0.01146	0.01084	1.05202
FWHM CIII] BC	5356	5075	5299	5299
FWHM SiIII] BC	5704	5416	5444	5444
FWHM AlIII BC	5708	5578	5674	5674
FWHM VBC	-	7024	7128	7128

**Notes.** <sup>(a)</sup> Model 1: Fit with only BCs as shown in Figure 5 (top panel). <sup>(b)</sup> Model 2: Fit with only a VBC in CIII] as described in section 3.2 (Figure 3, bottom panel). <sup>(c)</sup> Model 3: Fit with BC + VBCs in all three lines as Figure 15a. <sup>(d)</sup> Model 4: Synthetic model fit with BC+VBC in all three lines as Figure 15b.

AlIII profile, Pop. B shows symmetric shifts around 0; only Pop. xA show a median blueshift of  $-300 \text{ km s}^{-1}$  indicating a mixture of two unresolved components: a virialized plus an outflow component. The xA sub-sample showed an AlIII shift/FWHM ratio  $\sim 10$  to 15%, indicating that the displacement significantly affects the line width.

- The virial black hole mass estimations of our sample using the FWHM (AlIII) are consistent with the ones obtained with FWHM(CIII]), using the VP06 and M22 scale relations.
- Our xA sample (11 quasars) showed a broad consistency between the cosmological and virial luminosity computed with the equation derived by MS14; however, an excess in the virial luminosity with respect to the concordance one indicates that in this case the AlIII width is affected by a non-virial broadening.
- The comparison of the AlIII and a large numbers of CIV bootstrapped samples extracted from Shen et al. (2011) matching the luminosity distribution showed that the AlIII and CIV FWHM and shift distributions differ fundamentally, in the sense that the CIV $\lambda$ 1549 FWHM and shift distributions are much broader than those of AlIII. Shift amplitudes of CIV $\lambda$ 1549 are a factor  $\sim 10$  larger than the AlIII ones.
- Our single zone model proved that there is a very well defined region in the log plane  $n_H, U$  for the BC and BC+VBC models for the composite Pop. B spectra. As for the case of only VBC,  $n_H, U$  are not fully constrained. Nonetheless, the appearance of the blend and the intensity ratios of the components are consistent with the predominance of a virial velocity field, with a stratification of emission properties.

In conclusion, we can use the IILs AlIII and CIII] as a reliable surrogate mass estimator for Pops. A and B objects. Highly accreting quasars show smaller blueshifts (on average  $\ll 1000 \text{ km s}^{-1}$ ) compared to the ones observed in CIV, and the method discussed in this paper may provide slight  $M_{BH}$  overestimates by a factor  $\lesssim 2$  as described in Secs. 5.1 and 5.2.

*Acknowledgements.* D. Dultzin and C. A. Negrete acknowledge support from grant IN111422 PAPIIT UNAM. C. A. Negrete acknowledge support from

CONACyT project Paradigmas y Controversias de la Ciencia 2022-320020. The work of T. M. Buendia-Rios has been sponsored by CONACyT-Mexico through the Ph.D. scholarship No. 760641. Funding for the SDSS and SDSS-II has been provided by the Alfred P. Sloan Foundation, the Participating Institutions, the National Science Foundation, the U.S. Department of Energy, the National Aeronautics and Space Administration, the Japanese Monbukagakusho, the Max Planck Society, and the Higher Education Funding Council for England. The SDSS website is <http://www.sdss.org>. The SDSS is managed by the Astrophysical Research Consortium for the Participating Institutions listed at the <http://www.sdss.org>.

## References

- Bachev, R., Marziani, P., Sulentic, J. W., et al. 2004, ApJ, 617, 171
- Baldwin, J., Ferland, G., Korista, K., & Verner, D. 1995, ApJL, 455, L119+
- Baldwin, J. A., Ferland, G. J., Korista, K. T., Hamann, F., & LaCluyz, A. 2004, ApJ, 615, 610
- Bensch, K., del Olmo, A., Sulentic, J., Perea, J., & Marziani, P. 2015, Journal of Astrophysics and Astronomy, 36, 467
- Bentz, M. C., Walsh, J. L., Barth, A. J., et al. 2009, ApJ, 705, 199
- Bevington, P. R. & Robinson, D. K. 2003, Data reduction and error analysis for the physical sciences
- Boller, T., Brandt, W. N., & Fink, H. 1996, A&A, 305, 53
- Bon, N., Bon, E., Marziani, P., & Jovanović, P. 2015, Ap&SS, 360, 7
- Bon, N., Marziani, P., Bon, E., et al. 2020, A&A, 635, A151
- Boroson, T. A. 2002, ApJ, 565, 78
- Boroson, T. A. & Green, R. F. 1992, ApJS, 80, 109
- Capellupo, D. M., Netzer, H., Lira, P., Trakhtenbrot, B., & Mejía-Restrepo, J. 2016, MNRAS, 460, 212
- Coatman, L., Hewett, P. C., Banerji, M., & Richards, G. T. 2016, MNRAS, 461, 647
- Coatman, L., Hewett, P. C., Banerji, M., et al. 2017, MNRAS, 465, 2120
- Collin, S., Kawaguchi, T., Peterson, B. M., & Vestergaard, M. 2006, A&A, 456, 75
- Corbin, M. R. 1995, ApJ, 447, 496
- Dalla Bontà, E., Peterson, B. M., Bentz, M. C., et al. 2020, ApJ, 903, 112
- Decarli, R., Dotti, M., & Treves, A. 2011, MNRAS, 413, 39
- Deconto-Machado, A., del Olmo, A., Marziani, P., Perea, J., & Stirpe, G. 2021, Astronomische Nachrichten [https://onlinelibrary.wiley.com/doi/pdf/10.1002/asna.20210084]
- Denney, K. D. 2012, ApJ, 759, 44
- Denney, K. D., Peterson, B. M., Pogge, R. W., et al. 2010, ApJ, 721, 715
- Di Matteo, T., Croft, R. A. C., Springel, V., & Hernquist, L. 2003, ApJ, 593, 56
- Dong, X.-B., Wang, J.-G., Ho, L. C., et al. 2011, ApJ, 736, 86



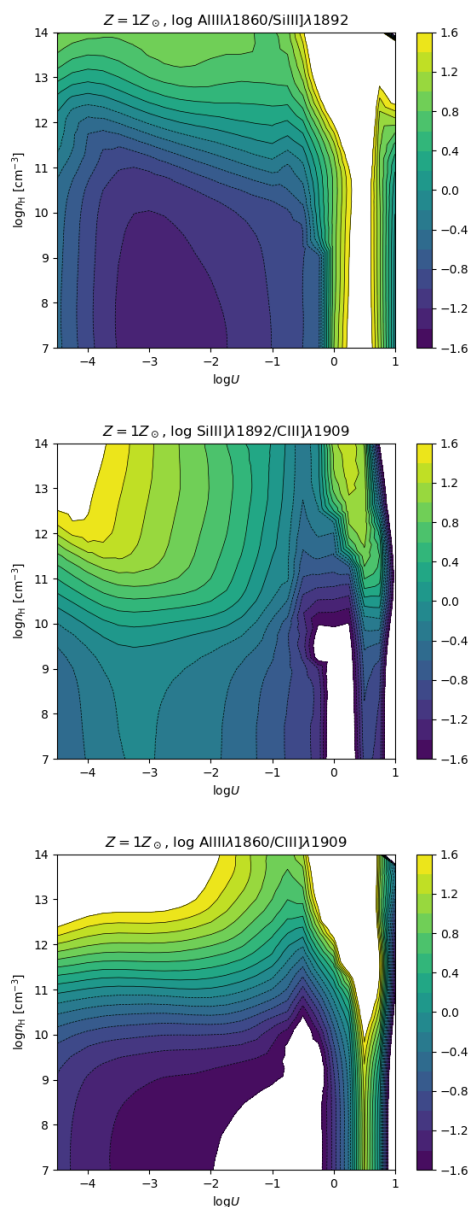


Fig. 16: From top to bottom, maps of intensity ratios as a function of ionisation parameter and Hydrogen number density:  $\log \text{AlIII}\lambda 1860/\text{SiIII}\lambda 1892$ ,  $\log \text{SiIII}\lambda 1892/\text{CIII}\lambda 1909$  and  $\log \text{AlIII}\lambda 1860/\text{CIII}\lambda 1909$ .

Du, P., Wang, J.-M., Hu, C., et al. 2016, *ApJ*, 818, L14  
 Feng, H.-C., Hu, C., Li, S.-S., et al. 2021, *ApJ*, 909, 18  
 Ferland, G. J., Chatzikos, M., Guzmán, F., et al. 2017, *Rev. Mexicana Astron. Astrofis.*, 53, 385  
 Ferland, G. J., Hu, C., Wang, J., et al. 2009, *ApJ*, 707, L82  
 Fraix-Burnet, D., Marziani, P., D’Onofrio, M., & Dultzin, D. 2017, *Frontiers in Astronomy and Space Sciences*, 4, 1  
 Francis, P. J., Hewett, P. C., Foltz, C. B., et al. 1991, *ApJ*, 373, 465  
 Gallagher, S. C., Everett, J. E., Abado, M. M., & Keating, S. K. 2015, *MNRAS*, 451, 2991  
 Gaskell, C. M. 1982, *ApJ*, 263, 79  
 Giustini, M. & Proga, D. 2019, *A&A*, 630, A94  
 Grupe, D., Wills, B. J., Leighly, K. M., & Meusinger, H. 2004, *AJ*, 127, 156  
 Hartig, G. F. & Baldwin, J. A. 1986, *ApJ*, 302, 64  
 Hewett, P. C. & Wild, V. 2010, *MNRAS*, 405, 2302  
 Johansson, S., Zethson, T., Hartman, H., et al. 2000, *A&A*, 361, 977  
 Komossa, S. & Xu, D. 2007, *ApJ*, 667, L33  
 Korista, K., Baldwin, J., Ferland, G., & Verner, D. 1997a, *ApJS*, 108, 401  
 Korista, K., Baldwin, J., Ferland, G., & Verner, D. 1997b, *ApJS*, 108, 401

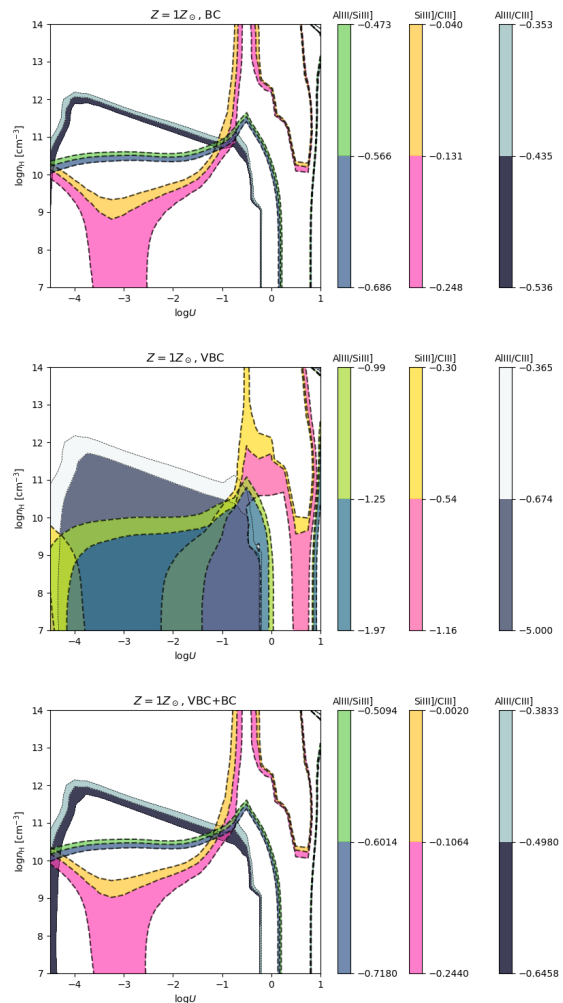


Fig. 17: Isophotes tracing the loci of the parameter plane ( $\log U$ ,  $\log n_{\text{H}}$ ) consistent with the observed intensity ratios  $\text{AlIII}\lambda 1860/\text{SiIII}\lambda 1892$ ,  $\text{SiIII}\lambda 1892/\text{CIII}\lambda 1909$  and  $\text{AlIII}\lambda 1860/\text{CIII}\lambda 1909$  (shown in log scale in the Figure). The crossing region defines the ( $U$ ,  $n_{\text{H}}$ ) parameter range consistent with the values of the three ratios. *Up*: BC only, *middle*: VBC, *bottom*: BC+VBC.

Kriss, G. 1994, in *Astronomical Society of the Pacific Conference Series*, Vol. 61, *Astronomical Data Analysis Software and Systems III*, ed. D. R. Crabtree, R. J. Hanisch, & J. Barnes, 437  
 Kuraszewicz, J., Wilkes, B. J., Czerny, B., & Mathur, S. 2000, *ApJ*, 542, 692  
 Kuraszewicz, J. K., Green, P. J., Crenshaw, D. M., et al. 2004, *ApJS*, 150, 165  
 La Mura, G., Di Mille, F., Ciroi, S., Popović, L. Č., & Rafanelli, P. 2009, *ApJ*, 693, 1437  
 Laor, A. 2000, *ApJ*, 543, L111  
 Laor, A., Fiore, F., Elvis, M., Wilkes, B. J., & McDowell, J. C. 1997, *ApJ*, 477, 93  
 Leighly, K. M. & Moore, J. R. 2004, *ApJ*, 611, 107  
 Li, S.-S., Yang, S., Yang, Z.-X., et al. 2021, *ApJ*, 920, 9  
 Lira, P., Botti, I., Kaspi, S., & Netzer, H. 2017, *Frontiers in Astronomy and Space Sciences*, 4, 71  
 Lira, P., Kaspi, S., Netzer, H., et al. 2018, *ApJ*, 865, 56  
 Liu, H. T., Feng, H. C., & Bai, J. M. 2017, *MNRAS*, 466, 3323  
 Lyke, B. W., Higley, A. N., McLane, J. N., et al. 2020, *ApJS*, 250, 8  
 Malkan, M. A. & Sargent, W. L. W. 1982, *ApJ*, 254, 22  
 Marconi, A., Axon, D. J., Maiolino, R., et al. 2009, *ApJ*, 698, L103  
 Martínez-Aldama, M. L., del Olmo, A., Marziani, P., et al. 2018, *A&A*, 618, A179  
 Martínez-Aldama, M. L., Del Olmo, A., Marziani, P., et al. 2018, *Frontiers in Astronomy and Space Sciences*, 4, 65

- Marziani, P., del Olmo, A., Negrete, C. A., et al. 2022, arXiv e-prints, arXiv:2205.07034
- Marziani, P., del Olmo, A., Perea, J., D’Onofrio, M., & Panda, S. 2020, *Atoms*, 8, 94
- Marziani, P., Dultzin, D., del Olmo, A., et al. 2021, in *Nuclear Activity in Galaxies Across Cosmic Time*, ed. M. Pović, P. Marziani, J. Masegosa, H. Netzer, S. H. Negu, & S. B. Tessema, Vol. 356, 66–71
- Marziani, P., Dultzin, D., Sulentic, J. W., et al. 2018, *Frontiers in Astronomy and Space Sciences*, 5, 6
- Marziani, P., Dultzin-Hacyan, D., & Sulentic, J. W. 2006, in *New Developments in Black Hole Research*, ed. P. V. Kreidler (Nova Press, New York), 123
- Marziani, P., Martínez Carballo, M. A., Sulentic, J. W., et al. 2016, *Ap&SS*, 361, 29
- Marziani, P., Olmo, A., Martínez-Aldama, M., et al. 2017, *Atoms*, 5, 33
- Marziani, P. & Sulentic, J. W. 2012, *The Astronomical Review*, 7, 33
- Marziani, P. & Sulentic, J. W. 2014, *MNRAS*, 442, 1211
- Marziani, P., Sulentic, J. W., Dultzin-Hacyan, D., Calvani, M., & Moles, M. 1996, *ApJS*, 104, 37
- Marziani, P., Sulentic, J. W., Negrete, C. A., et al. 2010, *MNRAS*, 409, 1033
- Marziani, P., Sulentic, J. W., Plauchu-Frayn, I., & del Olmo, A. 2013, *ApJ*, 764, 150
- Marziani, P., Sulentic, J. W., Zamanov, R., & Calvani, M. 2003a, *Memorie della Societa Astronomica Italiana*, 74, 490
- Marziani, P., Sulentic, J. W., Zwitter, T., Dultzin-Hacyan, D., & Calvani, M. 2001, *ApJ*, 558, 553
- Marziani, P., Zamanov, R. K., Sulentic, J. W., & Calvani, M. 2003b, *MNRAS*, 345, 1133
- Matsuoka, Y., Kawara, K., & Oyabu, S. 2008, *ApJ*, 673, 62
- McLure, R. J. & Jarvis, M. J. 2002, *MNRAS*, 337, 109
- Mediavilla, E., Jiménez-Vicente, J., Fian, C., et al. 2018, *ApJ*, 862, 104
- Mejía-Restrepo, J. E., Lira, P., Netzer, H., Trakhtenbrot, B., & Capellupo, D. 2017, *Frontiers in Astronomy and Space Sciences*, 4, 70
- Mejía-Restrepo, J. E., Lira, P., Netzer, H., Trakhtenbrot, B., & Capellupo, D. M. 2018, *Nature Astronomy*, 2, 63
- Mineshige, S., Kawaguchi, T., Takeuchi, M., & Hayashida, K. 2000, *PASJ*, 52, 499
- Moore, C. E. 1945, *Contributions from the Princeton University Observatory*, 20, 1
- Negrete, C. A., Dultzin, D., Marziani, P., & Sulentic, J. W. 2012, *ApJ*, 757, 62
- Negrete, C. A., Dultzin, D., Marziani, P., & Sulentic, J. W. 2013, *ApJ*, 771, 31
- Negrete, C. A., Dultzin, D., Marziani, P., & Sulentic, J. W. 2014, *ApJ*, 794, 95
- Netzer, H. 1977, *MNRAS*, 181, 89
- Netzer, H. 2015, *ARA&A*, 53, 365
- Netzer, H. & Marziani, P. 2010, *ApJ*, 724, 318
- Netzer, H. & Peterson, B. M. 1997, *Astronomical Time Series*, 85
- Panda, S., Martínez-Aldama, M. L., & Zajaček, M. 2019a, *Frontiers in Astronomy and Space Sciences*, 6, 75
- Panda, S., Marziani, P., & Czerny, B. 2019b, *ApJ*, 882, 79
- Peterson, B. M., Ali, B., Horne, K., et al. 1993, *ApJ*, 402, 469
- Peterson, B. M. & Wandel, A. 1999, *ApJ*, 521, L95
- Peterson, B. M. & Wandel, A. 2000, *ApJ*, 540, L13
- Petrucci, P. O., Gronkiewicz, D., Rozanska, A., et al. 2020, *A&A*, 634, A85
- Popović, L. Č., Kovačević-Dojčinović, J., & Marčeta-Mandić, S. 2019, *MNRAS*, 484, 3180
- Richards, G. T., Kruczek, N. E., Gallagher, S. C., et al. 2011, *AJ*, 141, 167
- Richards, G. T., Strauss, M. A., Fan, X., et al. 2006, *AJ*, 131, 2766
- Sadowski, A. 2011, arXiv e-prints, arXiv:1108.0396
- Salviander, S., Shields, G. A., Gebhardt, K., & Bonning, E. W. 2007, *ApJ*, 662, 131
- Schlafly, E. F. & Finkbeiner, D. P. 2011, *ApJ*, 737, 103
- Shen, Y. 2013, arXiv preprint arXiv:1302.2643
- Shen, Y. & Ho, L. C. 2014, *Nature*, 513, 210
- Shen, Y., Richards, G. T., Strauss, M. A., et al. 2011, *ApJS*, 194, 45
- Sigut, T. A. A. & Pradhan, A. K. 1998, *ApJ*, 499, L139
- Singh, K. P., Garmire, G. P., & Nousek, J. 1985, *ApJ*, 297, 633
- Sądowski, A., Narayan, R., McKinney, J. C., & Tchekhovskoy, A. 2014, *MNRAS*, 439, 503
- Small, T. A. & Blandford, R. D. 1992, *MNRAS*, 259, 725
- Snedden, S. A. & Gaskell, C. M. 2007, *ApJ*, 669, 126
- Śniegowska, M., Kozłowski, S., Czerny, B., Panda, S., & Hryniewicz, K. 2020, *ApJ*, 900, 64
- Śniegowska, M., Marziani, P., Czerny, B., et al. 2021, *ApJ*, 910, 115
- Sulentic, J. W., Bachev, R., Marziani, P., Negrete, C. A., & Dultzin, D. 2007, *ApJ*, 666, 757
- Sulentic, J. W., del Olmo, A., Marziani, P., et al. 2017, *A&A*, 608, A122
- Sulentic, J. W., Marziani, P., del Olmo, A., et al. 2014, *A&A*, 570, A96
- Sulentic, J. W., Marziani, P., & Dultzin-Hacyan, D. 2000a, *ARA&A*, 38, 521
- Sulentic, J. W., Marziani, P., Zamanov, R., et al. 2002, *ApJ*, 566, L71
- Sulentic, J. W., Marziani, P., Zwitter, T., Dultzin-Hacyan, D., & Calvani, M. 2000b, *ApJL*, 545, L15
- Sulentic, J. W., Zamfir, S., Marziani, P., & Dultzin, D. 2007, arXiv preprint arXiv:0709.2499
- Sulentic, J. W., Zwitter, T., Marziani, P., & Dultzin-Hacyan, D. 2000c, *ApJ*, 536, L5
- Sulentic, J. W., Zwitter, T., Marziani, P., & Dultzin-Hacyan, D. 2000d, *ApJL*, 536, L5
- Sun, J. & Shen, Y. 2015, *The Astrophysical Journal Letters*, 804, L15
- Tody, D. 1986, in *Society of Photo-Optical Instrumentation Engineers (SPIE) Conference Series*, Vol. 627, *Instrumentation in astronomy VI*, ed. D. L. Crawford, 733
- Vanden Berk, D. E., Richards, G. T., Bauer, A., et al. 2001, *AJ*, 122, 549
- Vestergaard, M. & Peterson, B. M. 2006, *ApJ*, 641, 689
- Vestergaard, M. & Wilkes, B. J. 2001, *ApJS*, 134, 1
- Vietri, G., Piconcelli, E., Bischetti, M., et al. 2018, *A&A*, 617, A81
- Walter, R. & Fink, H. H. 1993, *A&A*, 274, 105
- Wandel, A. & Petrosian, V. 1988, *ApJ*, 329, L11
- Wang, J. & Li, Y. 2011, *ApJ*, 742, L12
- Wang, J.-M., Du, P., Brotherton, M. S., et al. 2017, *Nature Astronomy*, 1, 775
- Wang, T., Brinkmann, W., & Bergeron, J. 1996, *A&A*, 309, 81
- Wills, B. J., Laor, A., Brotherton, M. S., et al. 1999, *ApJ*, 515, L53
- Wolf, J., Salvato, M., Coffey, D., et al. 2020, *MNRAS*, 492, 3580
- Zamanov, R., Marziani, P., Sulentic, J. W., et al. 2002, *ApJ*, 576, L9
- Zamfir, S., Sulentic, J. W., Marziani, P., & Dultzin, D. 2010, *MNRAS*, 403, 1759
- Zheng, W. & Sulentic, J. W. 1990, *ApJ*, 350, 512

## Appendix A: Extreme accretor sources multi-component fits

The results of line profile fitting for the 1900Å blend are shown in the following Figure A.1. Notes for some of the objects within the xA sub-sample:

- J152314.49+375928.9: One of the highest blueshift sources:  $\text{shift}(\text{AlIII}) = -849.96 \pm 25 \text{ km s}^{-1}$ , with a  $\text{FWHM}(\text{AlIII}) = 4000 \pm 400 \text{ km s}^{-1}$ . This source is also the one with an additional component in FeIII1914 due to the high amount of iron emission observed in the red side of CIII].
- J100827.67+210931.1: Brightest quasar with a  $\log L_{\text{bol}} = 47.06$ , with a  $\text{FWHM}(\text{AlIII}) = 3612 \pm 362 \text{ km s}^{-1}$  it give us also one of the most massive xA quasar with a  $\log M_{\text{BH}}(\text{AlIII}) = 8.92$ .
- J235157.59+003610.6: This object was affected by the host galaxy emission, it was fitted with positive continuum and a few absorption lines in the red side of SiIII]1892 and CIII]1909 are observed.
- J095531.45+174340.3: One of the brightest sources with a  $\log L_{\text{bol}} = 47.04$ , with a relatively high  $\text{shift}(\text{AlIII}) = -427 \pm 43 \text{ km s}^{-1}$ . This object has the highest Eddington ratio in the sub-sample,  $R_{\text{Edd}} = 1.34$ .
- J092612.68+202326.6: This object presented an AlIII redshift of  $262 \pm 27 \text{ km s}^{-1}$  with a  $\text{FWHM}(\text{AlIII}) = 3771 \pm 370$ .
- J003546.29-034118.2: Highest blueshifted source,  $\text{shift}(\text{AlIII}) = -1011.69 \pm 81 \text{ km s}^{-1}$ ,  $\text{FWHM}(\text{AlIII}) = 4194.93 \pm 342 \text{ km s}^{-1}$ . With a  $\delta \log L_{\text{vir}} = -0.75$ .

## Appendix B: Line fitting procedures and derived computations header table

Data obtained for this work and can be described as follows by number of columns in Table B.1:

- (1) file SDSS name,
- (2-5)  $z$  of this work obtained with  $[\text{OII}]\lambda 3728$  ( $\Delta z = z_{[\text{OII}]} - z_{\text{SDSS}}$ ) and the SDSS extracted values with errors,
- (6) signal-to-noise ratio around 1700Å,
- (7-10) continuum flux at 1700Å and its normalisation flux with errors,
- (11) assigned profile of the CIII]1909 line: Gaussian or Lorentzian, for xA sources it was added to the name the notation "xA"
- (12-13) power-law index -  $\alpha$  with error for REGION 1,
- (14-41) flux, equivalent width, FWHM, shift of AlIII1860, SiIII]1892 and CIII]1909 BC,
- (42-45) UV diagnostics ratios with errors,
- (46-69) flux and FWHM of NIII]1750, SiII1816, FeII(UV191), FeII(UV34), CIII]VBC and NC with errors obtained by `specfit`,
- (70) power-law index -  $\alpha$  for REGION 2,
- (71-74) flux and FWHM of  $[\text{OII}]\lambda 3728$  with errors,
- (75-80) continuum flux at 1350Å and pseudo-continuum flux at 3700Å with errors,
- (81-83) logarithmic line luminosity at 1860Å, 1892Å and 1909Å,
- (84-85) logarithmic bolometric luminosity,
- (86) FWHM using the luminosity-dependant criterion,
- (87-88) logarithmic black hole mass using CIII]1909 and AlIII1860,
- (89-92) eddington ratio using CIII]1909 and AlIII1860 with errors,
- (93-94) logarithmic virial luminosity for Pop. xA sources with errors

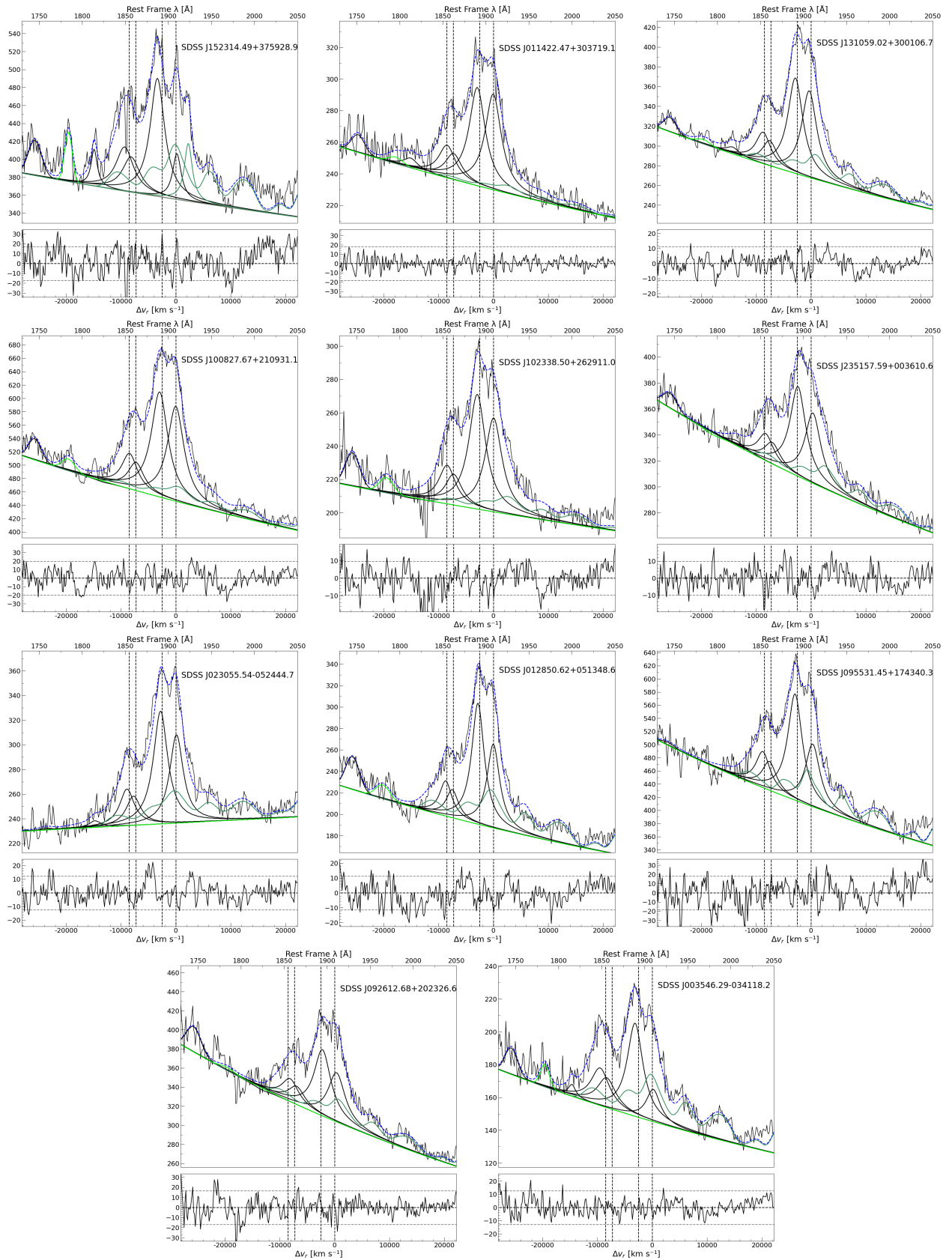


Fig. A.1: Analysis of the 1900Å blend as described in section 3.2 for the 11 xA sources in our work. Abscissa scales are rest-frame wavelength in Å. Ordinate scale is the specific flux. Black lines identify the BC of AlIIIλ1860, SiIIIλ1892 and CIIIλ1909. Dashed blue line is the multi-component model obtained by `specfit`. Green lines trace the adopted Fe II (pale) and Fe II template (dark).

Table B.1: Header description of the sample with individual measurements.

COL	Identifier	Type	Units	Description
1	SDSS	CHAR	NULL	File name
2	z	FLOAT	NULL	z for this work, measured using [OIII] $\lambda$ 3728 (see text)
3	z_ERR	FLOAT	NULL	z (this work) error
4	z_SDSS	FLOAT	NULL	z given by the SDSS database
5	z_SDSS_ERR	FLOAT	NULL	z given by the SDSS database error
6	SN	FLOAT	NULL	S/N Ratio measured around 1700Å
7	C1700	FLOAT	ergs s <sup>-1</sup> cm <sup>-2</sup> Å <sup>-1</sup>	Continuum Flux at 1700Å
8	C1700_ERR	FLOAT	ergs s <sup>-1</sup> cm <sup>-2</sup> Å <sup>-1</sup>	Continuum Flux at 1700Å error
9	N1700	FLOAT	NULL	Continuum normalisation at 1700Å
10	N1700_ERR	FLOAT	NULL	Continuum normalisation at 1700Å error
11	CIII_PROFILE	CHAR	NULL	CIII $\lambda$ 1909 BC Line Profile. G = Gaussian, L = Lorentzian
12	ALPHA_R1	FLOAT	NULL	Power Law Index - $\alpha$ in Region 1 (see text)
13	ALPHA_R1_ERR	FLOAT	NULL	Power Law Index - $\alpha$ error
14	FLUX_FEIII	FLOAT	10 <sup>-17</sup> ergs s <sup>-1</sup> cm <sup>-2</sup> Å <sup>-1</sup>	FeIII Flux
15	FLUX_FEIII_ERR	FLOAT	10 <sup>-17</sup> ergs s <sup>-1</sup> cm <sup>-2</sup> Å <sup>-1</sup>	FeIII Flux error
16	SHIFT_FEIII	FLOAT	Å	FeIII shift with respect to the Rest-frame
17	SHIFT_FEIII_ERR	FLOAT	Å	FeIII shift with respect to the Rest-frame error
18	EW_CIII	FLOAT	Å	CIII $\lambda$ 1909 BC Equivalent Width
19	EW_CIII_ERR	FLOAT	Å	CIII $\lambda$ 1909 BC Equivalent Width error
20	FLUX_CIII	FLOAT	10 <sup>-17</sup> ergs s <sup>-1</sup> cm <sup>-2</sup> Å <sup>-1</sup>	CIII $\lambda$ 1909 BC Flux
21	FLUX_CIII_ERR	FLOAT	10 <sup>-17</sup> ergs s <sup>-1</sup> cm <sup>-2</sup> Å <sup>-1</sup>	CIII $\lambda$ 1909 BC Flux error
22	SHIFT_CIII	FLOAT	km s <sup>-1</sup>	CIII $\lambda$ 1909 BC shift with respect to the Rest-frame
23	SHIFT_CIII_ERR	FLOAT	km s <sup>-1</sup>	CIII $\lambda$ 1909 BC shift with respect to the Rest-frame error
24	FWHM_CIII	FLOAT	km s <sup>-1</sup>	CIII $\lambda$ 1909 BC Full Width at Half Maximum
25	FWHM_CIII_ERR	FLOAT	km s <sup>-1</sup>	CIII $\lambda$ 1909 BC Full Width at Half Maximum error
26	EW_SIII	FLOAT	Å	SIII $\lambda$ 1892 Equivalent Width
27	EW_SIII_ERR	FLOAT	Å	SIII $\lambda$ 1892 Equivalent Width error
28	FLUX_SIII	FLOAT	10 <sup>-17</sup> ergs s <sup>-1</sup> cm <sup>-2</sup> Å <sup>-1</sup>	SIII $\lambda$ 1892 Flux
29	FLUX_SIII_ERR	FLOAT	10 <sup>-17</sup> ergs s <sup>-1</sup> cm <sup>-2</sup> Å <sup>-1</sup>	SIII $\lambda$ 1892 Flux error
30	SHIFT_SIII	FLOAT	km s <sup>-1</sup>	SIII $\lambda$ 1892 shift with respect to the Rest-frame
31	SHIFT_SIII_ERR	FLOAT	km s <sup>-1</sup>	SIII $\lambda$ 1892 shift with respect to the Rest-frame error
32	FWHM_SIII	FLOAT	km s <sup>-1</sup>	SIII $\lambda$ 1892 Full Width at Half Maximum
33	FWHM_SIII_ERR	FLOAT	km s <sup>-1</sup>	SIII $\lambda$ 1892 Full Width at Half Maximum error
34	EW_ALIII	FLOAT	Å	AlIII $\lambda$ 1860 Equivalent Width
35	EW_ALIII_ERR	FLOAT	Å	AlIII $\lambda$ 1860 Equivalent Width error
36	FLUX_ALIII	FLOAT	10 <sup>-17</sup> ergs s <sup>-1</sup> cm <sup>-2</sup> Å <sup>-1</sup>	AlIII $\lambda$ 1860 Flux
37	FLUX_ALIII_ERR	FLOAT	10 <sup>-17</sup> ergs s <sup>-1</sup> cm <sup>-2</sup> Å <sup>-1</sup>	AlIII $\lambda$ 1860 Flux error
38	SHIFT_ALIII	FLOAT	km s <sup>-1</sup>	AlIII $\lambda$ 1860 shift with respect to the Rest-frame
39	SHIFT_ALIII_ERR	FLOAT	km s <sup>-1</sup>	AlIII $\lambda$ 1860 shift with respect to the Rest-frame error
40	FWHM_ALIII	FLOAT	km s <sup>-1</sup>	AlIII $\lambda$ 1860 Full Width at Half Maximum
41	FWHM_ALIII_ERR	FLOAT	km s <sup>-1</sup>	AlIII $\lambda$ 1860 Full Width at Half Maximum error
42	AIII_SIII	FLOAT	NULL	UV Diagnostic ratio AlIII $\lambda$ 1860/SIII $\lambda$ 1892
43	AIII_SIII_ERR	FLOAT	NULL	UV Diagnostic ratio AlIII $\lambda$ 1860/SIII $\lambda$ 1892 error
44	CIII_SIII	DOUBLE	NULL	UV Diagnostic ratio CIII $\lambda$ 1909/SIII $\lambda$ 1892
45	CIII_SIII_ERR	FLOAT	NULL	UV Diagnostic ratio CIII $\lambda$ 1909/SIII $\lambda$ 1892 error
46	FLUX_NIII	FLOAT	10 <sup>-17</sup> ergs s <sup>-1</sup> cm <sup>-2</sup> Å <sup>-1</sup>	NIII $\lambda$ 1750 Flux
47	FLUX_NIII_ERR	FLOAT	10 <sup>-17</sup> ergs s <sup>-1</sup> cm <sup>-2</sup> Å <sup>-1</sup>	NIII $\lambda$ 1750 Flux err
48	FWHM_NIII	FLOAT	km s <sup>-1</sup>	NIII $\lambda$ 1750 Full Width at Half Maximum
49	FWHM_NIII_ERR	FLOAT	km s <sup>-1</sup>	NIII $\lambda$ 1750 Full Width at Half Maximum error
50	FLUX_SII	FLOAT	10 <sup>-17</sup> ergs s <sup>-1</sup> cm <sup>-2</sup> Å <sup>-1</sup>	SII $\lambda$ 1816 Flux
51	FLUX_SII_ERR	FLOAT	10 <sup>-17</sup> ergs s <sup>-1</sup> cm <sup>-2</sup> Å <sup>-1</sup>	SII $\lambda$ 1816 Flux error
52	FWHM_SII	FLOAT	km s <sup>-1</sup>	SII $\lambda$ 1816 Full Width at Half Maximum
53	FWHM_SII_ERR	FLOAT	km s <sup>-1</sup>	SII $\lambda$ 1816 Full Width at Half Maximum error
54	FLUX_FEII	FLOAT	10 <sup>-17</sup> ergs s <sup>-1</sup> cm <sup>-2</sup> Å <sup>-1</sup>	FeII Flux
55	FLUX_FEII_ERR	FLOAT	10 <sup>-17</sup> ergs s <sup>-1</sup> cm <sup>-2</sup> Å <sup>-1</sup>	FeII Flux error
56	FWHM_FEII	FLOAT	km s <sup>-1</sup>	FeII Full Width at Half Maximum
57	FWHM_FEII_ERR	FLOAT	km s <sup>-1</sup>	FeII Full Width at Half Maximum error

Table B.1: continued.

COL	Identifier	Type	Units	Description
58	FLUX_CIIINC	FLOAT	$10^{-17}$ ergs s <sup>-1</sup> cm <sup>-2</sup> Å <sup>-1</sup>	CIII]λ1909 NC Flux
59	FLUX_CIIINC_ERR	FLOAT	$10^{-17}$ ergs s <sup>-1</sup> cm <sup>-2</sup> Å <sup>-1</sup>	CIII]λ1909 NC Flux error
60	FWHM_CIIINC	FLOAT	km s <sup>-1</sup>	CIII]λ1909 NC Full Width at Half Maximum
61	FWHM_CIIINC_ERR	FLOAT	km s <sup>-1</sup>	CIII]λ1909 NC Full Width at Half Maximum error
62	FLUX_CIIIVBC	FLOAT	$10^{-17}$ ergs s <sup>-1</sup> cm <sup>-2</sup> Å <sup>-1</sup>	CIII]λ1909 VBC Flux
63	FLUX_CIIIVBC_ERR	FLOAT	$10^{-17}$ ergs s <sup>-1</sup> cm <sup>-2</sup> Å <sup>-1</sup>	CIII]λ1909 VBC Flux error
64	FWHM_CIIIVBC	FLOAT	km s <sup>-1</sup>	CIII]λ1909 VBC Full Width at Half Maximum
65	FWHM_CIIIVBC_ERR	FLOAT	km s <sup>-1</sup>	CIII]λ1909 VBC Full Width at Half Maximum error
66	FLUX_FE1914	FLOAT	$10^{-17}$ ergs s <sup>-1</sup> cm <sup>-2</sup> Å <sup>-1</sup>	FeIII]λ1914 Flux
67	FLUX_FE1914_ERR	FLOAT	$10^{-17}$ ergs s <sup>-1</sup> cm <sup>-2</sup> Å <sup>-1</sup>	FeIII]λ1914 Flux error
68	FWHM_FE1914	FLOAT	km s <sup>-1</sup>	FeIII]λ1914 Full Width at Half Maximum
69	FWHM_FE1914_ERR	FLOAT	km s <sup>-1</sup>	FeIII]λ1914 Full Width at Half Maximum error
70	ALPHA_R2	FLOAT	NULL	Power Law Index - α in Region 2 (see text)
71	FLUX_OII	FLOAT	$10^{-17}$ ergs s <sup>-1</sup> cm <sup>-2</sup> Å <sup>-1</sup>	[OII]λ3728 Flux
72	FLUX_OII_ERR	FLOAT	$10^{-17}$ ergs s <sup>-1</sup> cm <sup>-2</sup> Å <sup>-1</sup>	[OII]λ3728 Flux error
73	FWHM_OII	FLOAT	km s <sup>-1</sup>	[OII]λ3728 Full Width at Half Maximum
74	FWHM_OII_ERR	FLOAT	km s <sup>-1</sup>	[OII]λ3728 Full Width at Half Maximum error
75	C1350	FLOAT	$10^{-17}$ ergs s <sup>-1</sup> cm <sup>-2</sup> Å <sup>-1</sup>	Continuum Flux at 1350 Å
76	C1350_ERR	FLOAT	$10^{-17}$ ergs s <sup>-1</sup> cm <sup>-2</sup> Å <sup>-1</sup>	Continuum Flux at 1350 Å error
77	C3700	FLOAT	$10^{-17}$ ergs s <sup>-1</sup> cm <sup>-2</sup> Å <sup>-1</sup>	Pseudo-continuum Flux at 3700 Å
78	C3700_ERR	FLOAT	$10^{-17}$ ergs s <sup>-1</sup> cm <sup>-2</sup> Å <sup>-1</sup>	Pseudo-continuum Flux at 3700 Å error
79	C5100	FLOAT	$10^{-17}$ ergs s <sup>-1</sup> cm <sup>-2</sup> Å <sup>-1</sup>	Continuum Flux at 5100 Å
80	C5100_ERR	FLOAT	$10^{-17}$ ergs s <sup>-1</sup> cm <sup>-2</sup> Å <sup>-1</sup>	Continuum Flux at 5100 Å error
81	LOG_L1860	DOUBLE	ergs s <sup>-1</sup>	Logarithmic Line Luminosity at 1860 Å
82	LOG_L1892	DOUBLE	ergs s <sup>-1</sup>	Logarithmic Line Luminosity at 1892 Å
83	LOG_L1909	DOUBLE	ergs s <sup>-1</sup>	Logarithmic Line Luminosity at 1909 Å
84	LOG_L_BOL	DOUBLE	ergs s <sup>-1</sup>	Logarithmic bolometric Luminosity at 1700 Å
85	LOG_L_BOL_ERR	FLOAT	ergs s <sup>-1</sup>	Logarithmic bolometric Luminosity at 1700 Å error
86	FWHM_AB	DOUBLE	km s <sup>-1</sup>	FWHM <sub>AB</sub> using Sulentic et al. (2017) criterion
87	LOG_MBH_CIII	FLOAT	NULL	Logarithmic Black Hole Mass in solar masses of CIII]λ1909
88	LOG_MBH_AIII	FLOAT	NULL	Logarithmic Black Hole Mass in solar masses of AlIII]λ1860
89	REDD_CIII	FLOAT	NULL	Eddington Ratio using CIII]λ1909 line
90	REDD_CIII_ERR	FLOAT	NULL	Eddington Ratio using CIII]λ1909 line error
91	REDD_ALIII	FLOAT	NULL	Eddington Ratio using AlIII]λ1860 line
92	REDD_ALIII_ERR	FLOAT	NULL	Eddington Ratio using AlIII]λ1860 line error
93	LOG_L_VIR	DOUBLE	ergs s <sup>-1</sup>	Logarithmic Virial Luminosity for Pop. xA sources
94	LOG_L_VIR_ERR	FLOAT	ergs s <sup>-1</sup>	Logarithmic Virial Luminosity for Pop. xA sources error